Manipulation of Protein Aggregation and Aggregates Structures Using Nanoparticles on Brain-Mimicking Lipid Bilayers

뇌환경 모방 지질이중층 기반 나노입자를 이용한

단백질 응집현상 및 응집체 구조 조절

2017년 8월

서울대학교 대학원

화학부 무기화학

김 유 나

Abstract

Manipulation of Protein Aggregation and Aggregates Structures Using Nanoparticles on Brain-Mimicking Lipid Bilayers

Yuna Kim

Department of Chemistry

The Graduate School

Seoul National University

Cells in our body have several tens of microns in size and they respond to their microenvironment. Abnormal symptoms or extraordinary signs in the body are usually obtained by misleading cell-cell communication and signal transductions. More specifically, cell-cell communication and cell-extracellular matrix (ECM) interactions are generated at the cell membrane which makes physical barrier to shield intracellular components from the outside. Cell membranes provide a basic platform to investigate many biological processes including material transport, trafficking, and pathogenic pathways. In this regard, it is needed to develop bio-mimicking platforms and materials to understand the mechanism and progress of diseases perfectly. Microscale features could affect the whole-cell guidance and their responses, but nanoscale stimuli also have emerged as fascinating features for several decades. Subcellular structures such as lysosomes, lipids, transmembrane proteins, ion channels are of nanometer scales, so that nanomaterial could be one of attractive candidates to manipulate intra-and extracellular signals. Therefore, supported lipid

bilayers (SLBs) have been used as the cell membrane model and hybridized with various membrane-associated molecules to mimic living cells and envision molecular reactions on the membrane surface. For more precise investigation of complex biological processes, nanomaterials would be hybridized with the bio-mimicking system and have boosted the development of new platforms and methodologies. Therefore, Chapter 1 will explain manipulation of protein assemblies and aggregation process with a variety of nanomaterials and detection of biomolecular interactions on the cell membrane using SLB and nanomaterials.

In chapter 2, we studied the formation of various Aβ aggregate structures with gold nanoparticles (AuNPs) and brain total lipid extract-based supported lipid bilayer (brain SLB). Understanding and manipulating amyloid-β (Aβ) aggregation provide key knowledge and means for the diagnosis and cure of Alzheimer's disease (AD) and the applications of Aβ-based aggregation systems. The roles of AuNPs and brain SLB in forming Aβ aggregates were studied in real time, and the structural details of Aβ aggregates were monitored and analyzed with the dark-field imaging of plasmonic AuNPs that allows for long-term in situ imaging of Aβ aggregates with great structural details without further labeling. It was shown that the fluid brain SLB platform provides the binding sites for Aβ and drives the fast and efficient formation of Aβ aggregate structures and, importantly, large Aβ plaque structures (>15 μm in diameter), a hallmark for AD, were formed without going through fibril structures when Aβ peptides were co-incubated with AuNPs on the brain SLB. The dark-field scattering and circular dichroism-correlation data suggest that AuNPs were heavily involved with Aβ aggregation on the brain SLB and less α-helix, less β-sheet and more random coil structures were found in large plaque-like Aβ aggregates.

In chapter 3, we studied the effect of the size, shape, and surface charge of Au nanoparticles (AuNPs) on amyloid beta (Aβ) aggregation on a total brain lipid-based supported lipid bilayer (brain SLB), a fluid platform that facilitates Aβ-AuNP aggregation process. We found that larger

AuNPs induce large and amorphous aggregates on the brain SLB, whereas smaller AuNPs induce protofibrillar Aβ structures. Positively charged AuNPs were more strongly attracted to Aβ than negatively charged AuNPs, and the stronger interactions between AuNPs and Aβ resulted in fewer β-sheets and more random coil structures. We also compared spherical AuNPs, gold nanorods (AuNRs), and gold nanocubes (AuNCs) to study the effect of nanoparticle shape on Aβ aggregation on the brain SLB. Aβ was preferentially bound to the long axis of AuNRs and fewer fibrils were formed whereas all the facets of AuNCs interacted with Aβ to produce the fibril networks. Finally, it was revealed that different nanostructures induce different cytotoxicity on neuroblastoma cells, and, overall, smaller Aβ aggregates induce higher cytotoxicity. The results offer insight into the roles of NPs and brain SLB in Aβ aggregation on the cell membrane and can facilitate the understanding of Aβ-nanostructure co-aggregation mechanism and tuning Aβ aggregate structures.

Keyword: Alzheimer's disease, Amyloid β, Nanoparticle, Supported lipid bilayer, Self-assembly, Protein Aggregation, Secondary structure, Neurotoxicity

Student Number: 2011-20287

Contents

Chapter 1 : Introduction

Chapter 2. Amyloid β Aggregation with Gold Nanoparticles on Brain Lipid Bilayers

Chapter 3. How Do the Size, Charge and Shape of Nanoparticles Affect Amyloid β Aggregation on Brain Lipid Bilayer?

List of Figures

Chapter 1

Figure 1.1. CD spectra of 2.5O10¢7m BSA in its native state (curves a) and in bioconjugates at (A) pH 3.8, (B) pH 7.0, and (C) pH 9.0. AuNP concentration ranged from 2×10^{-10} to 1.1×10^{-9} M (curves b–e). (D) The helicity of BSA versus the concentration of AuNPs in the bioconjugates at pH 3.8 (curve a), 7.0 (curve b), and 9.0 (curve c). Ref. 7c.

Figure 1.2. Various experimental data involved in amyloid aggregation. (a) β_2m fibrillation co-incubated with different compositions and sizes of copolymer NPs. Smaller and more hydrophilic NPs promoted fibril formation. Ref 15. (b) Inhibition of Aβ fibrillation with polymeric NPs. Fibrillation kinetics monitored by the temporal development of thioflavin T binding in the absence (■) and in the presence of 50:50 (●), 65:35 (▲), 85:15 (▼), and 100:0 (◆) NiPAM:BAM polymeric particles at 37 °C. Aβ fibrillation is inhibited under larger particle/protein surface area ratio conditions and tight binding to polymeric NPs. Ref 17. (c) The dual effect of polystyrene NPs on Aβ fibrillation measured with 8 μM Aβ(M1-40) with 0 (black), 1 (blue), 17 (cyan), 55 (green), and 170 (red) μg/mL NPs; 2 μM Aβ(M1-42) with 0 (black), 10 (blue), 30 (cyan), 100 (green), and 300 (red) μg/mL NPs. Ref 21.

Figure 1.3. Transporter-mimicking system using proteins and SLBs. (a) Schematic showing proton transport in the bilayer incorporating a gramicidin A pore in the absence and presence of Ca^{2+} ions. (b) Time traces of normalized conductance of the SiNW device recorded as the solution was changed from pH 5 to 7 for an uncoated NW device (red trace), a device coated

with lipid bilayer incorporating gramicidin A pores (blue trace), and a device coated with the lipid bilayer incorporating gramicidin A pores in presence of Ca^{2+} ions (black trace). (c) Schematics showing the mechanism of voltage-gated proton transport in self-assembled ALM pores in the lipid bilayer. (d) Time traces of normalized conductance of the SiNW device held at gate bias of 0V recorded as the solution was changed from pH 6 to 9 for the uncoated nanowire (blue trace), coated nanowire (black trace), and the coated NW device incorporating ALM pores. (e) Time traces of a similar experiment recorded at gate bias of 0.15 V. Ref. 28 (f) Schematic illustration of passive transport of α-hemolysin and fluorescent images of the passive transport activity. (g) Continuous recording of the passive transport activity of 1 mg/ml α -hemolysin. (h) Histogram of the number of chambers versus the rate constant of passive transport, k. Ref. 29.

Figure 1.4. Self-assembly of neurodegenerative disease-related peptides using SLBs. (a) Schematic illustration for the model of GM1 ganglioside-clusters involved in formation of toxic Aβ species. Ref 31. (b) α-syn with α-helical structure intercalation into SLBs. Ref 32. (c) Illustration of protein binding model on the surface of lipid bilayers with high and low amounts of anionic lipids. Ref 33.

Figure 1.5. MDA-MB-231 cell adhesion upon varying RGD and ephrin-A1 presentation. (a) The fabrication of AuNPs arrays formed by BCML, SLB formation followed by selective labeling of the AuNPs and live-cellesperiments. SEM images of AuNPs arrays from five different samples with individual particle spacing varying between 58 and 151 nm (Scale bar, 200 nm). (b) MDA-MB-231 cells cultured on three different types of AuNPs-SLB hybridized

platforms. When RGD or ephrin-A1 is anchored to the lipid bilayer, the cells can interact and adhere to the substrate stably. Ref 34.

Chapter 2

Figure 2.1. Schematic illustration of Au nanoparticle-based Aβ aggregation and imaging assay on brain lipid bilayer. Au nanoparticles were used as both Aβ aggregation seeds and photostable imaging probes. The inset figures on the upper left are the fluorescence recovery after photobleaching images to confirm the fluidity of the brain SLB. Scale bar is 10 μm for the images.

Figure 2.2. AuNP aggregation and dark-field imaging analysis. (a) The surface plasmon band of aggregated AuNPs was red-shifted (red color in the dark-field image), compared to non-aggregated AuNPs (green color in the dark-field image, scale bar = 10 μm). Increase in salt concentration induces more nanoparticle aggregations (TEM images, scale bar = 200 nm). The dynamic light scattering and UV-Vis data further support inter-nanoparticle-coupling-based optical signal change. Color histogram graph shows the sum values of green and red colors in each salt concentration (please notice that the total sum value is same in every case). The green-to-red ratio is highest when there is no salt. (b) Comparison between piranha-etched glass and brain total lipid extract-based SLB as an Aβ aggregation platform. The images were obtained after 24-hr Aβ incubation at 37 °C. Scale bar is 20 μm for all the images. (c) The real-time optical signal tracking of fluorescent and dark-field images.

Figure 2.3. The time-lapse dark-field images of Aβ aggregates without and with AuNPs (a and b, respectively) on the brain SLB . Scale bars in all the images are 20 μm.

Figure 2.4. Optical and TEM image analysis on AuNP-Aβ aggregates. (a) Fluorescence-dark-field overlap images of plaque-like large Aβ aggregates. Fluorophore-labeled Aβ was incubated with AuNPs. Scale bars in the images are 20 µm. (b) TEM images of Aβ aggregates without AuNPs (left) and with AuNPs (right). Scale bars in both images are 100 nm. Incubation time is 48 hr for all the images.

Figure 2.5. The dark-field color, size and shape analysis of Aβ aggregates on the brain SLB. (a) Dark-field-based green and red color histogram for Aβ aggregates without AuNPs on the brain SLB. (b) Dark-field-based green and red color histogram for Aβ aggregates with AuNPs on the brain SLB. (c) Aβ size analysis after 24 hr and 48 hr incubation. ~100 Aβ aggregates were analyzed for each case (only average size values are shown). (d) The aspect ratio of Aβ aggregates in the dark-field images after 48 hr incubation.

Figure 2.6. The circular-dichroism-dark-field correlation measurements and the secondary structure analysis on Aβ aggregates. (a) The schematic diagram of the circular dichroism (CD) and dark-field co-analysis using a quartz cell. (b) The dark-field images of Aβ aggregates on the brain SLB that was formed on a quartz cell surface after 48 hr incubation. The scale bars in all images are 20 μm. (c) The CD results after 24 and 48 hr incubation for the condition

with and without AuNPs. Three replicate experiments were repeated for each case. (d) The secondary structure analysis on Aβ aggregates with the CD data.

Chapter 3

Figure 3.1. Schematic illustration of the formation of Aβ and gold nanoparticle (AuNP) co-aggregates on the total brain lipid-based supported lipid bilayer and cell viability assay with various Aβ aggregates. Depending on the size, charge, and shape of AuNPs, different Aβ aggregate structures can be formed.

Figure 3.2. The dark-field and TEM images of Aβ aggregates with various sizes of AuNPs [20-nm AuNPs (left), 50-nm AuNPs (middle), and 80-nm AuNPs (right)] on the brain SLB. The images were obtained after the co-incubation of Aβ and AuNPs for (a) 6 hr and (b) 48 hr. The inset figure in (b) shows a magnified image for the 20-nm AuNP case. It should be noted that the dark-field images of 20-nm AuNPs are difficult to be obtained. The scale bars in all the dark-field images are 10 μm and those in TEM images are 100 nm.

Figure 3.3. Analysis on the interactions between Aβ and AuNPs and the secondary structures of Aβ aggregates. The surface-enhanced Raman scattering (SERS) spectra of Aβ on the surfaces of (a) 20-nm AuNPs, (b) 50-nm AuNPs, and (c) 80-nm AuNPs with varying

incubation time. Circular-dichroism (CD) measurements and secondary structure analysis after co-incubation of Aβ and AuNPs for (d) 6 hr and (e) 48 hr. The error bars were calculated with three individual samples.

Figure 3.4. The dark-field and TEM images of Aβ-AuNPs co-aggregates with positively or negatively-charged AuNPs on the brain SLB after 6-hr and 48-hr co-incubation. Aβ and 40-nm AuNPs were co-incubated for (a) 6 hr and (b) 48 hr. The scale bars in the dark-field images are 10 μm whereas those in the TEM images are 100 nm.

Figure 3.5. Study on the interactions between Aβ and differently-charged AuNPs and secondary structural analysis of Aβ aggregates. (a) The SERS spectra from time-lapse incubation of Aβ and amine-AuNPs. (b) The SERS spectra of Aβ on the surface of citrate-AuNPs with varying incubation time. The CD spectra show the secondary structures of Aβ aggregates incubated with AuNPs for (c) 6 hr and (d) 48 hr. The error bars were calculated with three independent samples.

Figure 3.6. The dark-field and TEM images for Aβ aggregates incubated with AuNRs and AuNCs on the brain SLB. The image were obtained after (a) 6-hr incubation and (b) 48-hr incubation. The scale bars of the dark-field images are 10 μm and those of the TEM images are 100 nm.

Figure 3.7. Analyses on the interactions between Aβ and differently-shaped nanoparticles and secondary structural analysis of Aβ aggregates. The SERS signals were measured after time-lapse incubation for (a) AuNRs and (b) AuNCs. The CD spectra show the secondary structures of Aβ aggregates incubated with AuNRs or AuNCs for (c) 6 hr and (d) 48 hr. The error bars were calculated with three individual replicates.

Figure 3.8. Cell viability assay of Aβ aggregates formed after 6-hr and 48-hr incubation with SH-SY5Y neuroblastoma cells using CCK-8 assay. After 6-hr and 48-hr incubation of Aβ and Au nanostructures on the brain SLB, the collected Aβ aggregates were incubated with SH-SY5Y cells at a concentration of 1.0×10^4 cells/well in 96-well plates. The error bars were calculated with three individual replicates.

List of Tables

Chapter 1. Introduction

1.1 Introduction

In recent years, people have tried to diagnose diseases at an early stage and find a way to cure them completely. Cells in our body have several tens of microns in size and they respond to their microenvironment. Abnormal metabolism or symptoms in the body are usually obtained by misleading cell-cell communication and signal transductions. Cell-cell communication and cell-extracellular matrix (ECM) interactions are generated at the cell membrane which acts as a physical barrier to protect intracellular components from the outside. The cell membrane provides a basic platform inherently to investigate many biological processes including material transport, trafficking, and pathogenic pathways. In this respect, it is important to develop bio-mimicking platforms and materials to understand the mechanism and progress of diseases perfectly, and supported lipid bilayers (SLBs) could be a model membrane platform providing robust artificial cell membranes.[1] Moreover, microscale features could affect the whole-cell guidance and their responses, but nanoscale features could provoke more precise stimuli in the microenvironment. Subcellular structures including lysosomes, lipids, transmembrane proteins, ion channels have nanometer scales, so that nanomaterial could be one of appropriate candidates to control intra-and extracellular signals.[2] SLBs have been decorated with various membrane-associated molecules to mimic living cells and investigate biomolecular reactions on the membrane surface. For understanding more complex processes, nanomaterials would be hybridized with the bio-mimicking system and have boosted the development of new platforms and methodologies.

In this chapter, it will be introduced about manipulation of protein assemblies and aggregation process with a variety of nanomaterials and detection of biomolecular interactions on the cell membrane using SLB and nanomaterials.

1.2. Manipulation of Biomolecule Aggregation and Structures Using Nanoparticles

1.2.1. Introduction

Nanoparticles (NPs) possess large adsorption capacities, high surface area to volume ratios, the ability to bind other molecules to their surfaces, and strong physical properties. Modifying the surface of NPs with proteins can add biofunctionality and increase biocompatibility to enable their use in many biomedical fields, including biosensors, bioimaging, and the development of biocompatible materials.[3-5] When NPs are introduced into a physiological environment and come into contact with biological fluids, biomolecules can bind to the NP surface and form protein "corona" structures owing to exchange of low-affinity, high-abundance proteins that bind immediately to lower abundance proteins with a higher affinity for the NP surface. The binding of biomolecules to NPs is governed by protein–NP binding affinities, which depend on the size, shape, and surface characteristics of the NP, and is also affected by various forces, such as hydrodynamic force, electrodynamic force, electrostatic force, and solvent and polymer bridging at bio-nanointerfaces.[6, 7] Because, as mentioned above, the interactions between proteins and NPs can vary with the size, curvature, and surface properties of the NP,[8] and protein aggregation can be affected by the interactions. Protein aggregation is a hallmark of many diseases, including

Alzheimer's and Parkinson's diseases.[9] The interactions between NPs and proteins are also important for understanding the fate of NPs when NPs are inside human bodies. This section introduces recent studies on the conformational changes of proteins on the surfaces of NPs and the influence of the physicochemical properties of the NPs on protein–NP interactions,. As proteins adsorb onto the surface of NPs, they tend to undergo partial denaturation followed by structural changes, which induce protein–NP aggregation or protein expansion and assembly with the NPs. Herein, it will be discussed how the properties of NPs affect protein–NP aggregation and protein self-assembly mechanisms.

1.2.2. Influence of NPs on Conformational Changes of Proteins and Their Aggregation

Proteins can undergo conformational changes on the surface of NPs, and several properties of NPs are involved with it.[6] Li Shang *et al.* [7c] reported that bovine serum albumin (BSA) has the capacity to change its conformational state more readily on the surface of gold nanoparticles (AuNP) and that BSA in AuNP-BSA bio-conjugates undergoes substantial conformational changes at both the secondary and tertiary structure levels. They found that the bio-conjugates contained different BSA isomeric forms at pH 3.8, 7.0, and 9.0, respectively. Figure 1.1 shows the CD spectra of BSA in its native state and in bio-conjugates with different concentrations of AuNPs at pH 3.8 (Figure 1.1a), 7.0 (Figure 1.1b), and 9.0 (Figure 1.1c). The conformational changes of BSA were mainly evaluated by its α-helical structure. Increasing the concentration of AuNPs in the bio-conjugates resulted in a decrease in α-helix ellipticity at both 208 and 222 nm, and these two peaks approached each other in the range of 208 and 222 nm. This phenomenon demonstrates the loss of α-helical structure owing to conjugation with AuNPs and the possible conformational transition from α-helix to β-sheet structure in the bio-conjugates. Furthermore, as can be seen in the Figure 1.1d, the

helicity of BSA decreased gradually with an increase in the AuNPs concentration, it could be related to either a stronger structural change of BSA at the surface of NP. And the obtained slope values K (Table 1.1) followed an order of pH 9.0 > pH 7.0 > pH 3.8, which means that the decrease of the helical structure in the bio-conjugates was strongly pH-dependent. FT-IR spectroscopy was also used to study changes in the secondary structure of proteins; the FT-IR data in this study showed an increase in β-sheet and β-turn structures and a decrease in α-helical BSA structures in the bio-conjugates. In result, conformational changes in BSA are greatly influenced by the interaction with AuNPs and the pH of the medium.

Protein adsorption characteristics can also be controlled by changing NP surface parameters such as chemistry,[10] size, and curvature.[11] Jiang *et al.*[12] demonstrated that the conformational changes in cytochrome C (cyt c) were influenced by the size of the colloidal AuNPs and the coverage of cyt c adsorption on the NPs. Interestingly, they found that adsorption of cyt c onto 2-4 nm AuNPs induced a more compact conformation than 16 nm AuNPs. These findings indicate that different forces could affect the adsorption of cyt c onto the AuNPs; electrostatic interactions caused the adsorption of cyt c onto 16 nm AuNPs, whereas hydrophobic interactions were probably the main driving force in the case of the 2-4 nm AuNPs. The different degrees of cyt c coverage on the NPs were related to conformational changes in the adsorbed cyt c. In contrast, Klein[13] stated that the curvature of smaller NPs may completely suppress the adsorption of certain larger proteins. Thus, the size and chemical composition of the NPs constitute important parameters in determining the composition of the protein-NP conjugates.

1.2.3. Influence of NPs on the self-assembly of proteins.

β_2-microglobulin (β_2m), a factor involved in dialysis-related amyloidosis, and neurodegenerative disease related proteins such as amyloid β (Aβ) and α-synuclein (αS) tend to form fibrils when their local concentration increases. Fibril formation is a nucleation-dependent process and critical nucleus formation is the key rate-determining step followed by rapid fibrillation.[14]

Linse *et al.*[15] suggested that NPs could enhance the appearance of a critical nucleus by decreasing lag time for nucleation (Figure 1.2a). They controlled the size and hydrophobicity of copolymer particles along with changing the β_2m and salt concentration in solution. The presence of NPs provided a higher local concentration of monomers inducing appropriate conformational change and leading to a dramatic increase in the rate of fibrillation. At low salt concentrations, smaller and more hydrophilic NPs accelerated fibril formation, whereas larger and more hydrophilic NPs promoted protein fibrillation at high salt concentration. NP hydrophobicity is involved in the association and dissociation kinetics, and β_2m exhibit weaker binding onto the NP surface.[15] Other studies have shown that AuNPs could influence the aggregation of an Aβ fragment that contains 11 amino acids. Aβ-(25-35) (Aβ_{25-35}) fragment is comprised of positively charged amino acids and neutral amino acids and is thus adsorbed onto the surface of the AuNPs due to strong electrostatic interactions. The aggregation of Aβ_{25-35} with AuNPs exhibited an enhanced ThT fluorescence signal compared to that of Aβ_{25-35} without the AuNPs, indicating that the aggregation of Aβ_{25-35} with AuNPs produced more β-sheet structures. In addition, in a solution of Aβ_{25-35} with AuNPs, oligomers tend to adsorb on the surface of AuNPs and form short fibrils and bundled short fibrils but no long fibrils. AuNPs could act as the nucleus for the fibrillation of Aβ_{25-35} and control the mechanism of Aβ_{25-35} aggregation.[16]

In contrast, other studies have stated that NPs inhibit protein fibrillation or

aggregation. Although the local protein concentration is increased and nucleation commences on the NP surface, tight binding or the large particle/protein surface area ratio hinder protein aggregation (Figure 1.2b). For example, it has been shown that tight interactions between Aβ monomers and NPs lead to unfavorable fibrillation conditions by blocking the binding site for peptide-peptide interactions thus increasing the length of time required to form sub- and near-critical nuclei. Because of the higher kinetic fibrillation barrier, fibril growth rate was retarded when co-incubated with copolymer NPs.[17] In addition, when peptides are bound at high levels to the NP surface, modification of the NP surface could play a role in the fibrillation process. For instance, when 2-4-nm diameter CdTe quantum dots (QDs) were modified with two different types of ligands, the increasing number of hydrogen bonds formed between the QD ligands and amino acids in the Aβ sequence prevented self-assembly and fibrillation.[18] In particular, smaller AuNPs composed of a few tens of Au atoms and ligands were more likely to inhibit β2m fibrillation; thus, AuNP binding hinders interactions with other proteins, resulting in a potential inhibition of fibrillation.[19] Studies conducted with five different types of mutants demonstrated that acceleration or inhibition of fibril formation is highly dependent on the intrinsic properties of the mutant proteins. In mutants with high stability and a low aggregation rate, fibril formation was accelerated; in contrast, when low stability and high aggregation rate mutants were co-incubated with the NPs, fibrillation was inhibited.[20] Another study also showed that polystyrene NPs have a dual effect on Aβ fibrillation dependent on the ratio between peptide and particle concentrations (Figure 1.2c). The transition between acceleration and inhibition is not a continuous process, therefore no catalysis process is observed and fibrillation is inhibited when NP concentration becomes higher than the turnover concentration.[21]

Protein self-assembly in the presence or absence of NPs is greatly influenced not only by the

properties of the proteins such as their intrinsic stability and aggregation rate, but also by the physicochemical properties of NPs together with the size and concentration of the NPs that determines the peptide/NP ratio.

1.3. Controlling Biomolecular Interactions on SLB

1.3.1. Introduction

In nature, cells take advantage of a membrane to make physical barrier between intra-and extracellular compartments and to shield their components from the outside environment. The cell membrane is highly complex system consisting of two-ply sheet of leaflets id molecules and many kinds of various biomolecules. Natural cell membranes are considered as two dimensional liquid where proteins and lipid can more freely, so they provide high degree of lateral dynamics, flexibility, and complexity. Moreover, the cell membrane plays an important role in cell-cell communication, signal transduction, and transport and also, lipid translocation between leaflets affects biological functions such as cell fusion, coagulation, and apoptosis.[22] Cells can delicately sense and respond to external nanoscale features in living system. Cell membrane receptors reside at the interface between a cell and its extracellular matrix (ECM), so that they can transduce chemical and physical signals from outside to inside. Those extracellular stimuli influence on cell adhesion, proliferation, migration, and differentiation, which evoke the importance of ECM mimicking system to study nanoscale sensing capacity of cells.[23] Therefore, there have been many attempts to mimic the complexity of the cell membrane, ECM and their process. Among the various strategies to fabricate multi-molecular biological structure, supported lipid bilayer (SLB) has been widely used as a model cell membrane. SLB consists of phospholipid bilayers where a

variety of proteins and ligands can be embedded or anchored and it has high degree of lateral mobility, flexibility, and ordering.[24] SLB as a model phospholipid membrane allows to envisage biological at the cellular lever and to study membrane components in native cell membranes, so it is an attractive platform to mimic ECM-cell and cell-cell interactions. Especially, the lipid composition regulates domains of membrane that is also driven by lipid-protein, protein-protein interactions as well as the interaction between cytoskeleton and the membrane, so SLB can offer great opportunity to investigate the regulation of cellular biomechanical properties.[25] Otherwise, nanopatterning also affords unique means to mimic extracellular nanoenvironments and control it easily. Nanoscale stimuli are important in that subcellular structures are nano-sized and consist of various biomolecules. Integrins, a cell surface receptor, recognize specific ligand molecules within ECM and the integrin and ligand conjugation activate cell cytoskeleton formation. Hundreds of different types of proteins will assemble into a three-dimensional cross-linked structures and this phenomenon is called focal adhesion (FA).[26] Cytoskeletons are composed of filamentous protein assembly and stretch to the nucleus. Thus, FAs will exert physical forces to the cell nucleus and ECM, so these forces make cells possible to sense their microenvironment.[23] By engineering the interface through nanopatterning, we could control formation of FAs and physical forces which spontaneously affecting cell activation and function.

Herein, we describe recent studies that develop diverse bio-mimicking platforms and manipulate biomolecule interactions with nanostructure on the platform. Based on those platforms, we can unravel how cells recognize their environment and control their behaviors.

1.3.2. Detection of Membrane Proteins and Transporter Activity on SLB

Membrane proteins make up over 60% of known disease markers and 20-30% of genes

encoded in proteins. Therefore, people have been interested in membrane protein detection and the functions at the membrane. SLB was formed on heavily doped silicon nanowires (SiNWs) and α-hemolysin proteins were doped on the SLB. α-hemolysin proteins formed functional pores in the SLB, so specific transport though the pore made it possible to recover the Faradic current partially.[27] And also, Gramicidin A, a transmembrane protein, was also incorporated to the SLB and SiNW hybrid plarform, which resulted in $Fe(CN)_6^{4-}$ transport and chemically-gated ion transport (Figure 1.3a-e). Moreover, alamethicin was introduced to the hybrid system and alamethicin formed ion channels in the SLB by spontaneous insertion of alamethicin helix bundles. The helices could tilt enough to penetrate the membrane completely at the positive membrane potentials, so small monovalent cations could diffuse though the functional open pores.[28] More recently, free standing SLB was formed on nano-to micron-size arrays and α-hemolysin and F_0F_1-ATP synthase were fabricated onto the SLB (figure 1.3f-h). They stably launched on the SLB and form passive or active transport, so that sensitive and quantitative biological assays were developed.[29]

Membrane transporters could be key drug targets because they are involved in cellular metabolism, excretion of drugs, and homeostasis of ions, neutrients and solutes. Despite their important roles, membrane proteins have not been deeply studied due to the lack of suitable techniques and membrane-mimicking platforms. We will overcome these challenges using membrane protein-SLB hybridized system.

1.3.3 Assembly of Disease-Related Proteins on SLB

Several diseases occurred by abnormal aggregation of transmembrane proteins or peptide self-assembly and these phenomena are highly related to neurodegenerative diseases. Alzheimer's disease, Parkinson's disease, and Huntington disease are relatively well known

neurodegenerative disorders and it has been accepted that specific peptide affects neuronal cytotoxicity during peptide self-assembly. People have adopted that the peptides form self-assembled structures on the lipid bilayer, so that the effect and process of self-assembly on lipid bilayer has become more important.

M. C. Rheinstadter and co-workers tried to uncover an interaction between anionic lipid membrane and Aβ and they also found that cholesterol and melatonin components influenced on the interaction. The full length $A\beta_{1-42}$ embedded in the hydrocarbon core of anionic lipid bilayers, but the short length of $A\beta_{25-35}$ showed two populations such as membrane-bound states at the anionic lipid head groups with parallel aligned to the membrane and embedded states in the bilayer center. As increasing the percentage of cholesterol in the lipid bilayer, $A\beta_{25-35}$ more strongly interacted with the lipid bilayers and displaced cholesterol molecules to the plaques. However, addition of melatonin decreased the membrane-bound states of $A\beta_{25-35}$. [30] Besides, gangliosides same as glycosphingolipids could affect $A\beta_{1-42}$ conformational changes and self-assembly as shown in figure 1.4a. Monosialogangliosides (GM1) strongly interact with $A\beta_{1-42}$ and the ratio between $A\beta_{1-42}$ and GM1 showed different results in terms of secondary structural changes of $A\beta_{1-42}$. At low $A\beta_{1-42}$:GM1 ratio, $A\beta_{1-42}$ produced α-helix conformation, but it preferred β-sheet structures at high $A\beta_{1-42}$:GM1 ratio resulting in self-assembly of $A\beta_{1-42}$ and fibril formation.[31] Because $A\beta_{1-42}$ is produced from amyloid precursor protein that is a transmembrane protein, it has two domains; transmembrane domain and extracellular domain. We can assume that the interaction between lipid bilayer and $A\beta_{1-42}$ inherit from this feature.

The second most neurodegenerative disease, Parkinson's disease (PD) is involved in α-synuclein (α-syn) aggregation and α-syn self-assemblies are of β-sheet rich structures. Due to neurotoxicity of α-syn self-assembly, many researchers have studied α-syn and lipid

10

bilayer interaction. It has been discovered that α-syn binding to lipid bilayer affected their structures and thickness (Figure 1.4b). Because of strong interaction between α-syn and anionic lipids, α-syn binds to the head group of lipids and forms α-helix conformation. Then, α-syn could intercalate into the membrane followed by reduction in lipid bilayer thickness. Even though the thickness of lipid bilayers decreases, stability and density of the membrane are not changed. Therefore, binding of a peptide to lipid bilayers affect to secondary structures of the peptides and lipid thickness for further peptide aggregation.[32] This phenomenon could occur on negatively charged phospholipid bilayers more frequently due to binding tendency of α-syn and the binding of α-syn to membrane was deeply examined by J. S. Hovis and co-workers (Figure 1.4c). When increasing the amount of anionic phospholipids or α-syn on SLB, the propensity of α-syn to cluster on the membrane increases. α-syn likely binds to anionic lipds and induces clustering of the lipids. Based on clustered anionic lipids, more α-syn binding occurs and this makes it possible to α-syn conformational changes and self-assembly. And also, divalent metal ions (e.g. Ca^{2+}) stimulate anionic lipid clustering by lipid demixing, which influence on α-syn clusting and conformation changes into β-sheet.[33]

1.3.4. Controlling Cell Adhesion and Migration by nanostructure-tethered SLB

More recently, defined assays of AuNPs were fabricated on SLB by Spatz and co-workers.[34] By using block copolymer micelle nanolithography (BCMN), they could manipulate the array spacing and figure and 7 nm AuNPs were uniformly conjugated onto the glass. The range of spacing was from 58 nm to 151 nm and AuNPs were used as nanopattern after SLB formation on the glass as shown in figure 1.5a. The spacing and density of AuNPs did not affect a lateral mobility of SLB and they could modify the surface of AuNPs with several types of peptides. Thereafter, MDA-MB-231, human breast cancer cell line, were introduced on this

platform and MDA-MB-231 was able to reside on the SLB when ephrin-A1 interacting with a receptor at the surface of the cell were modified on AuNPs (Figure 1.5b). This proved that cells could interact with other cell membrane with specific ligand-receptor interactions.[35] As mentioned before, SLB is of great lateral mobility and this feature could make biomolecule moiety onto the SLB by altering lipid and peptide composition. Fluorophore linked cell receptor interacting ligand was conjugated with AuNP and this nanoprobe was tethered onto the SLB through streptavidin and biotin interaction. Because of AuNPs, fluorescence was quenched as the distance between AuNP and fluorophore decreased. In that sense, fluorescence signals could be great tool to detect physical forces between cell and the extracellular environment. When cells tightly adhered to the SLB by receptor clustering, fluorescence occurred due to cytoskeletal tension. Salaita and co-workers developed highly sensitive cell tension-detecting system and they obtained piconewton(pN) traction forces.[36]

1.4. References

1. Y. Lee, H. Lee and J. –M. Nam, *NPG Asia Materials*, **2013**, 5, e48

2. M. Dalby et al., *Nature Materials*, **2014**, 13, 558-570

3. a) Y. Liu, K. Yehl, Y. Narui and K. Salaita, *Journal of the American Chemical Society* **2013**, *135*, 5320-5323; b) Y. Liu, R. Medda, Z. Liu, K. Galior, K. Yehl, J. P. Spatz, E. A. Cavalcanti-Adam and K. Salaita, *Nano letters* **2014**, *14*, 5539-5546; c) W. Xu, X. Xue, T. Li, H. Zeng and X. Liu, *Angewandte Chemie International Edition* **2009**, *48*, 6849-6852; d) S. M. Kang, I. S. Choi, K.-B. Lee and Y. Kim, *Macromolecular Research* **2009**, *17*, 259-264.

4. Y. Yang, Q. Shao, R. Deng, C. Wang, X. Teng, K. Cheng, Z. Cheng, L. Huang, Z. Liu and

X. Liu, *Angewandte Chemie International Edition* **2012**, *51*, 3125-3129.

5. R. Jin, *Angewandte Chemie International Edition* **2008**, *47*, 6750-6753.

6. a) M. Lundqvist, J. Stigler, T. Cedervall, T. Berggård, M. B. Flanagan, I. Lynch, G. Elia and K. Dawson, *ACS nano* **2011**, *5*, 7503-7509; b) L. Fei and S. Perrett, *International journal of molecular sciences* **2009**, *10*, 646-655; c) L. Shang, Y. Wang, J. Jiang and S. Dong, *Langmuir* **2007**, *23*, 2714-2721.

7. a) A. Sasidharan, J. E. Riviere and N. A. Monteiro-Riviere, *Journal of Materials Chemistry B* **2015**, *3*, 2075-2082; b) L. Zhang, Q. Feng, J. Wang, S. Zhang, B. Ding, Y. Wei, M. Dong, J.-Y. Ryu, T.-Y. Yoon and X. Shi, *ACS nano* **2015**, *9*, 9912-9921; c) J. Sun, L. Zhang, J. Wang, Q. Feng, D. Liu, Q. Yin, D. Xu, Y. Wei, B. Ding and X. Shi, *Advanced Materials* **2015**, *27*, 1402-1407.

8. P. Roach, D. Farrar and C. C. Perry, *Journal of the American Chemical Society* **2006**, *128*, 3939-3945.

9. a) C. A. Ross and M. A. Poirier, **2004**; b) F. M. LaFerla, K. N. Green and S. Oddo, *Nature Reviews Neuroscience* **2007**, *8*, 499-509; c) D. J. Irwin, V. M.-Y. Lee and J. Q. Trojanowski, *Nature Reviews Neuroscience* **2013**, *14*, 626-636; d) C. A. Ross, E. H. Aylward, E. J. Wild, D. R. Langbehn, J. D. Long, J. H. Warner, R. I. Scahill, B. R. Leavitt, J. C. Stout and J. S. Paulsen, *Nature Reviews Neurology* **2014**, *10*, 204-216.

10. a) S. Srivastava, A. Verma, B. L. Frankamp and V. M. Rotello, *Advanced Materials* **2005**, *17*, 617-621; b) P. Roach, D. Farrar and C. C. Perry, *Journal of the American Chemical Society* **2005**, *127*, 8168-8173; c) L.-C. L. Huang and H.-C. Chang, *Langmuir* **2004**, *20*, 5879-5884; d) D. Hobora, S. Imabayashi and T. Kakiuchi, *Nano Lett* **2002**, *2*, 1021-1025; e) C. C. Dupont-Gillain, C. Fauroux, D. Gardner and G. Leggett, *Journal of Biomedical Materials Research Part A* **2003**, *67*, 548-558; f) B. G. Keselowsky, D. M. Collard and A. J. García, *Biomaterials* **2004**, *25*, 5947-5954.

11. a) M. Lundqvist, I. Sethson and B.-H. Jonsson, *Langmuir* **2004**, *20*, 10639-10647; b) A. A. Vertegel, R. W. Siegel and J. S. Dordick, *Langmuir* **2004**, *20*, 6800-6807.

12. X. Jiang, J. Jiang, Y. Jin, E. Wang and S. Dong, *Biomacromolecules* **2005**, *6*, 46-53.

13. J. Klein, *Proceedings of the National Academy of Sciences* **2007**, *104*, 2029-2030.

14. V. L. Colvin and K. M. Kulinowski, *Proceedings of the National Academy of Sciences* **2007**, *104*, 8679-8680.

15. S. Linse, C. Cabaleiro-Lago, W.-F. Xue, I. Lynch, S. Lindman, E. Thulin, S. E. Radford and K. A. Dawson, *Proceedings of the National Academy of Sciences* **2007**, *104*, 8691-8696.

16. Q. Ma, G. Wei and X. Yang, *Nanoscale* **2013**, *5*, 10397-10403.

17. C. Cabaleiro-Lago, F. Quinlan-Pluck, I. Lynch, S. Lindman, A. M. Minogue, E. Thulin, D. M. Walsh, K. A. Dawson and S. Linse, *Journal of the American Chemical Society* **2008**, *130*, 15437-15443.

18. H.-M. Chan, L. Xiao, K.-M. Yeung, S.-L. Ho, D. Zhao, W.-H. Chan and H.-W. Li, *Biomaterials* **2012**, *33*, 4443-4450.

19. G. Brancolini, D. Toroz and S. Corni, *Nanoscale* **2014**, *6*, 7903-7911.

20. C. Cabaleiro-Lago, O. Szczepankiewicz and S. Linse, *Langmuir* **2012**, *28*, 1852-1857.

21. C. Cabaleiro-Lago, F. Quinlan-Pluck, I. Lynch, K. A. Dawson and S. Linse, *ACS chemical neuroscience* **2010**, *1*, 279-287.

22. J. V. Weerd, M. Karperien, and P. Jonkheijm, *Advanced Healthcare Materials,* **2015**, *4*, 2743–2779

23. K. Ye, X. Wang, L. Cao, S. Li, Z. Li, L. Yu, and J. Ding, *Nano Letters,* **2015**, 15, 7755, 4720-4729

24. J. Brinkmann, E. Cavatorta, S. Sankaran, B. Schmidt, J. V. Weerd and P. Jonkheijm, *Chemical Society Reviews,* **2014** , *43* , 4449-4469

25. D. Lingwood, and K. Simons, *Science,* **2010** , *327* , 46

26. B. Geiger, J. P. Spatz and A. D. Bershadsky, *Nature Reviews Molecular Cell Biology,* **2009**, 10, 1, 21-33

27. J. A. Martinez, N. Misra, Y. Wang, P. Stroeve, C. P. Grigoropoulos, and A. Noy, Nano letters, 2009, 9, 3, 1121-1126

28. N. Misraa, J. A. Martineza, S. -C. J. Huang, Y. Wanga, P. Stroevec, C. P. Grigoropoulosb, and A. Noy, *Proceedings of the National Academy of Sciences,* 2009,106, 33, 13780–13784

29. R. Watanabe, N. Soga, D. Fujit, K. V. Tabata, L. Yamauchi, S. H. Kim, D. Asanuma, M. Kamiya, Y. Urano, H. Suga, and H. Noji, *Nature Communications*, **2014**, 5, 4519

30. H. Dies, L. Toppozini, M. C. Rheinstadter, *Plos One*, **2014**, 9, 6, e99124

31. a) A. Kakio, S. Nishimoto, K. Yanagisawa, Y. Kozutsumi and K. Matsuzaki, *Biochemistry*, **2002**, 41, 7385–7390, b) K. Ikeda, T. Yamaguchi, S. Fukunaga, M. Hoshino and K. Matsuzaki, *Biochemistry*, **2011**, 50, 6433–6440.

32. H. Hahl, I. Moller, I. Kiesel, S. Campioni, R. Riek, D. Verdes, and S. Seeger, *ACS Chemical Neuroscience*, **2015**, 6, 374−379

33. A. P. Pandey, F. Haque, J. -C. Rochet, and J. S. Hovis, *Biophysical Journal***, 2009,** 96, 2 540–551

34. R. Glass , M. Moller , J. P. Spatz , *Nanotechnology* **2003** , *14* , 1153 .

35. T. Lohmuller, S. Triffo, G. P. O'Donoghue, Q. Xu , M. P. Coyle, J. T. Groves, *Nano Letters,.* **2011**, *11*, 4912

36. V. P.-Y. Ma, Y. Liu, L. Blancheld, H. Su, B. D. Evavold, and K.Salaita*, Nano Letters*, **2016**, 16, 4552−4559
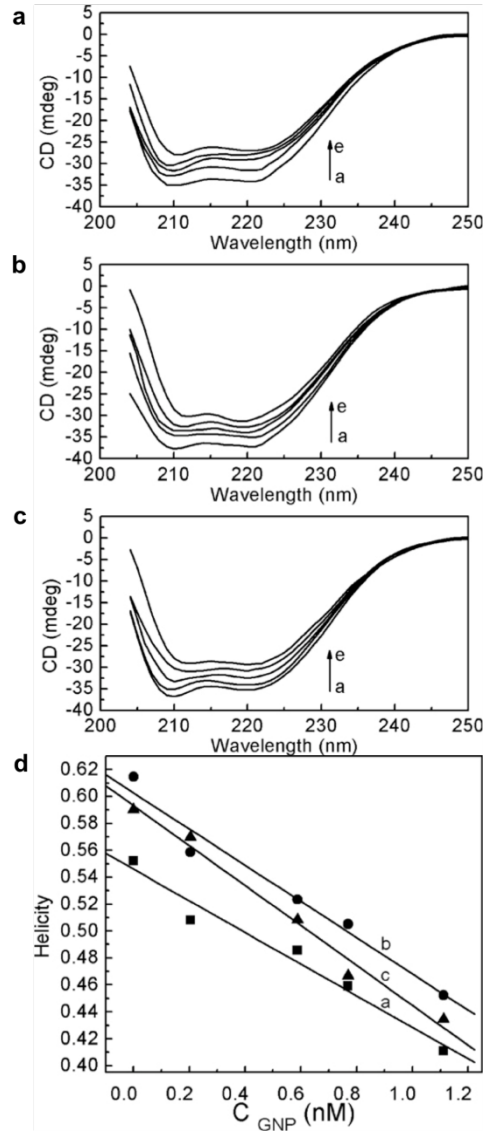
Figure 1.1. CD spectra of 2.5×10^{-7} M BSA in its native state (curves a) and in bioconjugates at pH 3.8 (a), pH 7.0 (b), and pH 9.0 (c). AuNP concentration ranged from 2×10^{-10} to 1.1×10^{-9} M (d). The helicity of BSA versus the concentration of AuNPs in the bioconjugates at pH 3.8 (curve a), 7.0 (curve b), and 9.0 (curve c). Ref. 7c.
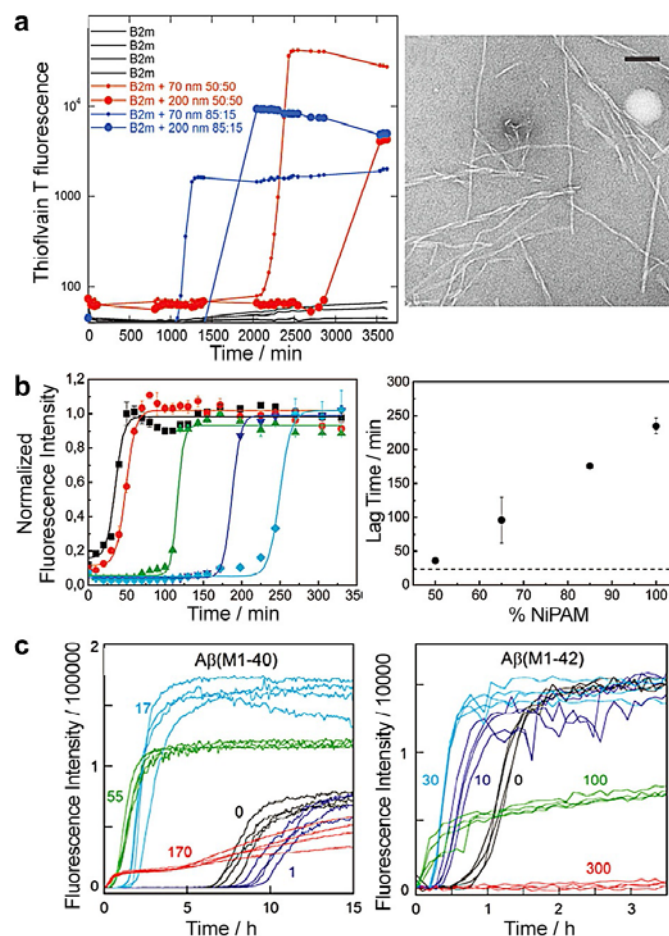
Figure 1.2. Various experimental data involved in amyloid aggregation. (a) β_2m fibrillation co-incubated with different compositions and sizes of copolymer NPs. Smaller and more hydrophilic NPs promoted fibril formation. Ref 15. (b) Inhibition of Aβ fibrillation with polymeric NPs. Fibrillation kinetics monitored by the temporal development of thioflavin T binding in the absence (■) and in the presence of 50:50 (●), 65:35 (▲), 85:15 (▼), and 100:0 (◆) NiPAM:BAM polymeric particles at 37 °C. Aβ fibrillation is inhibited under larger particle/protein surface area ratio conditions and tight binding to polymeric NPs. Ref 17. (c) The dual effect of polystyrene NPs on Aβ fibrillation measured with 8 μM Aβ(M1-40) with 0 (black), 1 (blue), 17 (cyan), 55 (green), and 170 (red) μg/mL NPs; 2 μM Aβ(M1-42) with 0 (black), 10 (blue), 30 (cyan), 100 (green), and 300 (red) μg/mL NPs. Ref 21.
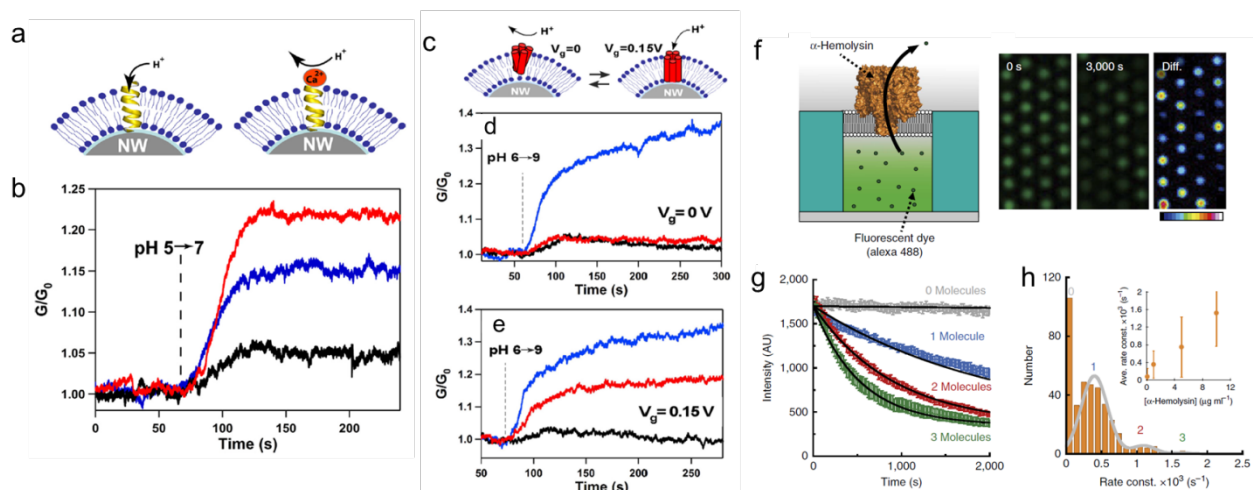
Figure 1.3. Transporter-mimicking system using proteins and SLBs. (a) Schematic showing proton transport in the bilayer incorporating a gramicidin A pore in the absence and presence of Ca^{2+} ions. (b) Time traces of normalized conductance of the SiNW device recorded as the solution was changed from pH 5 to 7 for an uncoated NW device (red trace), a device coated with lipid bilayer incorporating gramicidin A pores (blue trace), and a device coated with the lipid bilayer incorporating gramicidin A pores in presence of Ca^{2+} ions (black trace). (c) Schematics showing the mechanism of voltage-gated proton transport in self-assembled ALM pores in the lipid bilayer. (d) Time traces of normalized conductance of the SiNW device held at gate bias of 0V recorded as the solution was changed from pH 6 to 9 for the uncoated nanowire (blue trace), coated nanowire (black trace), and the coated NW device incorporating ALM pores. (e) Time traces of a similar experiment recorded at gate bias of 0.15 V. Ref. 28 (f) Schematic illustration of passive transport of α-hemolysin and fluorescent images of the passive transport activity. (g) Continuous recording of the passive transport activity of 1 mg/ml α -hemolysin. (h) Histogram of the number of chambers versus the rate constant of passive transport, k. Ref. 29.
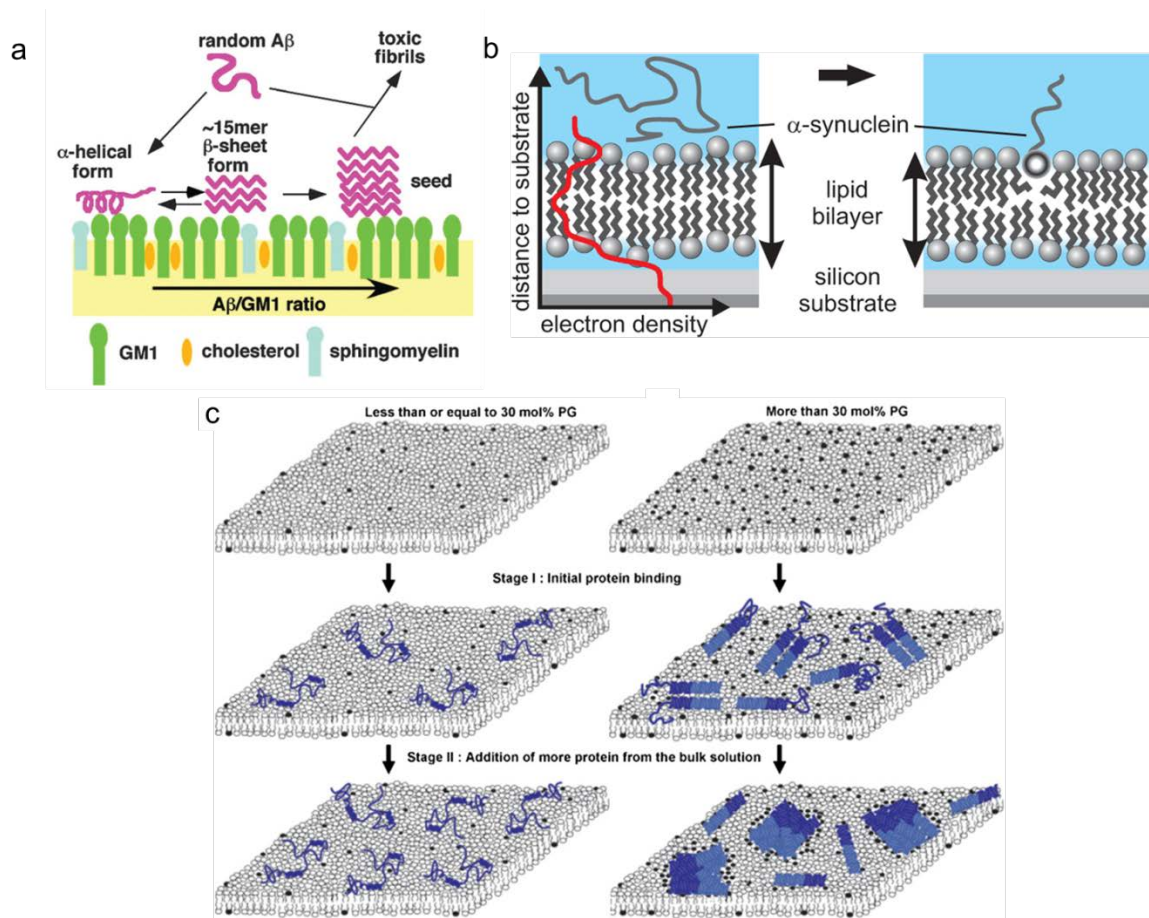
Figure 1.4. Self-assembly of neurodegenerative disease-related peptides using SLBs. (a) Schematic illustration for the model of GM1 ganglioside-clusters involved in formation of toxic Aβ species. Ref 31. (b) α-syn with α-helical structure intercalation into SLBs. Ref 32. (c) Illustration of protein binding model on the surface of lipid bilayers with high and low amounts of anionic lipids. Ref 33.
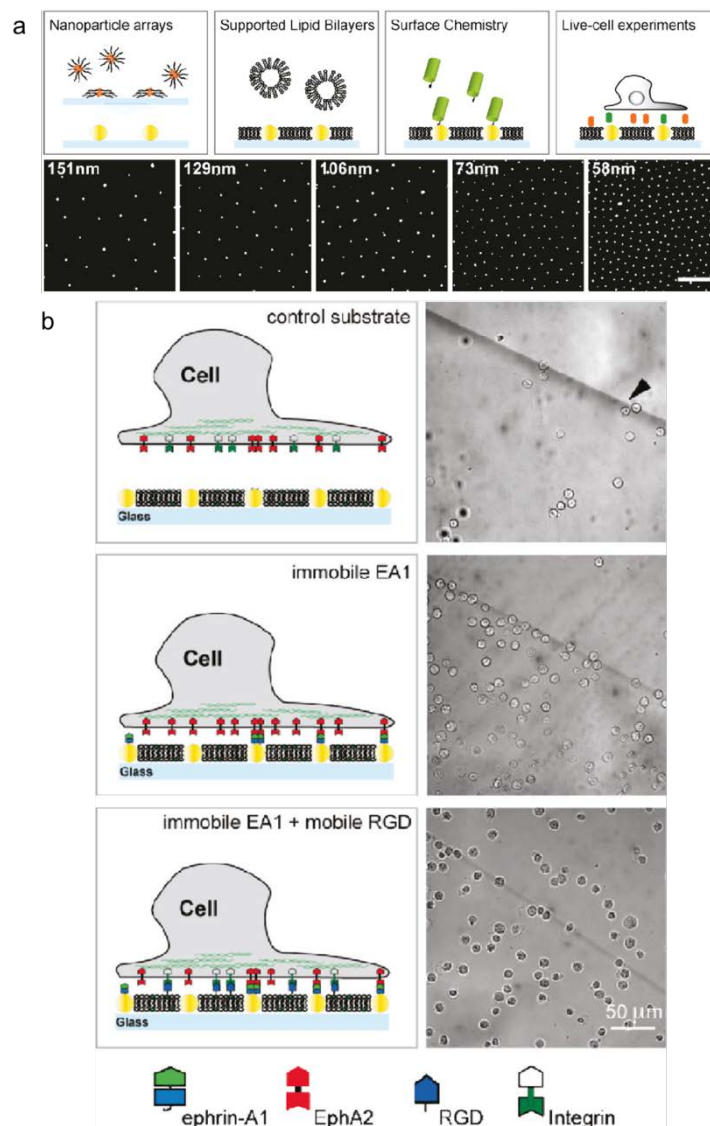
Figure 1.5. MDA-MB-231 cell adhesion upon varying RGD and ephrin-A1 presentation. (a) The fabrication of AuNPs arrays formed by BCML, SLB formation followed by selective labeling of the AuNPs and live-cellesperiments. SEM images of AuNPs arrays from five different samples with individual particle spacing varying between 58 and 151 nm (Scale bar, 200 nm). (b) MDA-MB-231 cells cultured on three different types of AuNPs-SLB hybridized platforms. When RGD or ephrin-A1 is anchored to the lipid bilayer, the cells can interact and adhere to the substrate stably. Ref 34.

t [h]	Citrate–Au [mV]	Lipoic acid–Au [mV]	Citrate–Ag [mV]	Lipoic acid–Ag [mV]
0	−11.2±3.4	−19.8±2.4	−25.9±1.9	−33.4±3.1
6	−12.7±2.6	−15.7±2.1	−21.4±2.6	−30.2±2.8
12	−11.6±3.7	−13.8±3.8	−21.6±2.5	−29.1±4.0
24	−10.9±2.8	−12.4±4.1	−17.3±3.3	−20.1±3.6
t [h]	Citrate–Au–HSA [mV]	Lipoic acid–Au–HSA [mV]	Citrate–Ag–HSA [mV]	Lipoic acid–Ag–HSA [mV]
0	−7.91±2.9	−9.77±3.7	10.8±2.5	−12.7±2.13
6	−8.74±2.3	−9.63±1.1	11.6±3.3	−12.4±2.14
12	−8.63±1.2	−8.53±2.1	−10.68±3.0	−11.8±3.21
24	−9.04±3.8	−10.68±3.7	−9.6±2.1	−11.6±4.4
t [h]	Citrate–Au–IgG [mV]	Lipoic acid–Au–IgG [mV]	Citrate–Ag–IgG [mV]	Lipoic acid–Ag–IgG [mV]
0	0.15±0.2	0.42±0.4	0.34±0.23	0.46±0.5
6	0.24±0.8	0.50±0.13	0.32±0.1	0.52±0.4
12	0.39±0.4	0.58±0.1	0.36±0.24	0.58±0.5
24	0.35±0.13	0.66±0.12	0.42±0.06	0.66±0.3

Table 1.1. Time-dependent zeta-potential analysis of NPs coated with citrate and lipoic acid in PBS, NP–HAS corona, and NP–IgG corona.

Chapter 2. Amyloid β Aggregation with Gold Nanoparticles on Brain Lipid Bilayer

2.1. Introduction

Amyloid-β_{1-42} (Aβ) aggregates are the hallmarks for Alzheimer's disease (AD) - AD is the most common age-related neurodegenerative disorder disease.[1] Although understanding the formation mechanism of large Aβ aggregate structures such as Aβ plaque from small soluble oligomeric, protofibrillar and fibrillar Aβ species is the stepping stone to diagnose and cure AD, the pathway to large Aβ aggregates is still not completely understood and highly controversial.[2] It was reported that cell membrane can play roles in Aβ aggregation-based neurodegeneration mechanism. The formation of ion channel on cell membrane, activation of signaling pathway, induction of oxidative stress on lipids of cell membrane, and recruitment of cellular factors in cell could be involved with the mechanism. It is likely that different pathways operate differently depending on whether the Aβ accumulates intra- or extracellularly.[3] However, the role of cell membrane for Aβ aggregation has not been thoroughly and systematically studied. Conventional Aβ aggregation assay is typically performed on a biologically irrelevant environment such as glass substrate.[4] This could be critical because it is known that membrane components such as cholesterol, anionic lipids and gangliosides are involved with Aβ assembly process and it has been reported that Aβ aggregate structures can be formed on extracellular membrane and brain parenchyma in nature.[5, 6] Another important point in Aβ aggregation is the roles of other materials such as nanostructures. It was recently shown that nanoparticles can play important roles in forming protein aggregates including amyloid fibrils via inducing or preventing protein misfolding.[7-

[10] However, the roles of nanometer-sized particles for the formation of large Aβ aggregates such as Aβ plaque and the exact formation pathways of various Aβ aggregates are largely unclear. It will be especially beneficial to use plasmonic nanoparticles such as gold nanoparticles (AuNPs) because non-bleaching and non-blinking light-scattering from these particles can be stably detected by the dark-field microscopy.[11,12] This is a highly beneficial feature because conventional fluorescence-based imaging methods are using fluorescent amyloidophilic dyes, Congo red and thioflavin T that have intrinsic limitations in reliable quantification, time-dependent structure monitoring and structural sensitivity [13-17] due to photobleaching, photoblinking and inconsistent signal intensity of fluorescent dyes.

Herein, we used plasmonic AuNPs as both nanometer-sized seeds and photostable imaging labels for forming and imaging Aβ aggregates on the brain total lipid extract-based supported lipid bilayer (brain SLB) that offer a fluid Aβ binding and assembling surface (Figure 2.1). Large Aβ aggregates including Aβ plaque, extracellular deposits of fibrils and amorphous aggregates of Aβ [18], were artificially formed and imaged with AuNPs on the brain SLB, and the roles of AuNPs and brain SLB in large Aβ aggregation were analytically studied. Plasmonic AuNPs can be structural substrates for altering Aβ structures and efficiently inducing large aggregate structures, and, at the same time, light-scattering signals from these particles can be directly detected by the dark-field microscopic method.[19] There will be more and stronger plasmonic couplings between AuNPs when more AuNPs are more densely packed, and stronger plasmonic coupling between AuNPs generates change in the dark-field color from green to red. This straightforward color change from photostable NPs can be utilized to analyze Aβ aggregates quantitatively in real time. Further, the brain SLB mimics a cell membrane environment in brain, offers a fluid substrate that allows for lateral mobility of lipids and lipid-tethered components, and is useful in investigating important

23

biological processes such as receptor clustering on a controllable and analyzable platform.[20, 21] Therefore, this aggregation and imaging platform allows for studying the roles of nanometer-sized seeds and brain cell membrane-mimicking SLB platform in inducing and understanding Aβ aggregate structures in a quantitative and real-time manner.

It was reported that nanoparticles, which offer large surface area and alter protein structures on their surface, can enhance the rate of protein fibirillation by shortening the lag phase for nucleation.[22] Our Aβ assay results show that AuNPs can be densely incorporated in Aβ aggregates and drive faster formation of larger Aβ aggregates without going through Aβ fibrillar structures for the eventual formation of large Aβ plaque-like structures. Importantly, large plaque structures were not formed without the aid of AuNPs. The results suggest that nanometer-sized seeds can play roles in altering the Aβ structure and assembly pathway on the brain SLB that laterally assemble Aβ peptides. To the best of our knowledge, this is the first example that induced the formation of large Aβ plaque structures using nanostructures without going through Aβ fibril structures on a lipid platform.

2.2. Experimental Section

Lipid vesicle preparation.

Small unilamellar vesicles (SUV, 100 nm diameter) of 98 mol % brain total lipid extract and 2 mol % NBD-PC (1-oleoyl-2-{6-[(7-nitro-2-1,3-benzoxadiazol-4-yl)amino]hexanoyl}-*sn*-glycero-3-phosphocholine) were formed by the extrusion method. Lipids (Avanti, Alabaster, AL, USA) were dissolved in chloroform and dried by evaporation with a rotary evaporator for 10 min. The lipid films were resuspended in deionized water (1 mL) and incubated overnight at 4 ˚C. The concentration of resulted lipids was 1 mg/mL. This lipid suspensions

were then extruded through a 100 nm polycarbonate membrane filter (Avanti, Alabaster, AL, USA) 15 times using a mini-extruder (Avanti, Alabaster, AL, USA). The resulting lipid vesicles were stored at 4 ˚C prior to use.

Initial solubilization of Aβ peptides.

The lyophilized-amyloid β-protein (Aβ$_{1-42}$) (Bachem AG, Bubendorf, Switzerland) was stored at -80 ˚C and diluted in DMSO (Sigma, Saint Louis, MO, USA) before use. This Aβ$_{1-42}$ solution (250 μM) was added to 300 μL of 10 mM phosphate buffer (PB, pH 7.4), which resulted in 330 μL Aβ solution. The resulting solution was centrifuged at 11000 rpm for 15 min in order to precipitate pre-aggregated Aβ oligomers. In this experiment, we used 100 μL of the supernatant that contained Aβ peptide monomers for each sample.

Preparation of supported lipid bilayer and Aβ aggregating condition.

A supported lipid bilayer was formed on a piranha-etched glass coverslip by the vesicle fusion and rupture method. In short, microscopic coverslips (Fisher Scientific, Pittsburgh, PA, USA) were soaked in piranha solution (3:1= concentrated sulfuric acid / 30 % hydrogen peroxide) for 20 min, thoroughly rinsed with deionized water, and then dried with a stream of nitrogen. The SUV suspension was mixed 3:1 (v/v) with phosphate-buffered saline (Gibco, Carlsbad, CA, USA), and 200 μL of the resulting solution was placed onto a plastic Petri dish. Next, the coverslip was placed on the droplet for 30 min at room temperature. The Petri dish was submerged in deionized water to remove excess vesicles. The SLB was then set in the well-slide (slide glass chamber, Live Cell Instrument, Seoul, South Korea) as a sandwich configuration with another coverslip. The dark-field chambers containing lipid bilayer in deionized water were washed with 400 μL of 10 mM phosphate buffer (PB, pH 7.4) for the optimized conditions of Aβ fibril growth. Finally, 100 μL of Aβ solution was added to the

newly formed SLB. Immediately after the addition of Aβ solution, the chamber was incubated at 37˚C, 5.0 % CO_2 for 48 hrs. The piranha etched glass was inserted into the chamber and then covered with another glass. 400 µL of 10 mM phosphate buffer (PB, pH 7.4) was injected to flow through the space between two glass slides. Subsequently, 100 µL of Aβ solution, prepared by the explained process, was also put into this chamber followed by incubation for 48 hrs at 37˚C, 5.0 % CO_2.

The co-incubation process of Aβ with AuNPs.

The co-incubation experiment was performed in order to find out difference in Aβ assembly structures, and we followed the same steps for making dark-field chambers. However, in case of Aβ solution preparation, the composition was altered by diluting the thawed aliquot with 270 µL of 10 mM phosphate buffer (PB, pH 7.4) as followed by centrifuging this solution at 11000 rpm for 15min and adding 30 µL of 50 pM AuNP solution. The total volume was also 330 µL which means that dilution ratio of Aβ aliquot did not change, and the supernatant of this Aβ solution was composed of AuNPs and Aβ monomers. After 100 µL of this supernatant was put into each dark-field chamber, total 6 chambers were incubated at 37˚C, 5.0 % CO_2 for 2, 4, 8, 12, 24, 48 hours respectively.

Image acquisition and processing.

Dark-field microscopy was performed using a 200 inverted microscope (Carl Zeiss, Oberkochen, Germany) equipped with a dark-filed condenser (NA=1.4, oil-immersion) and a white light illumination from a 100 W halogen lamp. Firstly, the scattering images of Aβ fibrils were taken using a 40X objective lens (NA= 0.8) (Axiovert 200M, Carl Zeiss, Oberkochen, Germany), then the same procedure was repeated subsequently to the deposition of the 50nm AuNPs (Ted Pella, Inc., Redding, CA, USA) (50 pM) to investigate the role of

AuNPs in the perspective of image enhancers.

Aβ immunostaining. After incubation for 48 hr to form Aβ aggregation, the samples were incubated with PBS solution containing 3% bovine serum albumin (BSA) (Sigma, Saint Louis, MO, USA) and anti- Aβ 1-16 antibody (Covance, Princeton, NJ, USA) for 60 min. Next, the substrates were washed twice by blocking buffer (3% BSA in 10 mM PB) injection. For fluorescence detection, FITC-conjugated-anti mouse secondary antibody (abcam, Cambridge, Cambridgeshire, UK) in 3% BSA solution was added to chamber. The sample was incubated for 1 h at room temperature without exposing to light. We decanted the secondary antibody solution and washed with phosphate buffer solution in the dark. Finally, we took the images of Aβ using florescence microscopy with the same exposure time to every image. (40X; Axiovert 200M, Carl Zeiss)

Characterization of AuNP aggregation.

Salt condition affects the aggregation of AuNPs, which also induces red shift in UV-Vis spectrum.[46] Varying the amount of NaCl such as 0, 1, 2, and 4 µmole in 50nm AuNP solution, their UV-Vis spectra were obtained, and then the size of aggregated particles was measured using DLS. Firstly, 50µL of the first sample that is pure 50nm AuNP solution was put into a cuvette, and the UV-Vis spectrum was collected by UV-Vis spectroscopy (Agilent 8453E, Agilent, Santan Clara, CA, USA). The UV-Vis spectra of other samples were also taken by following the same procedure. After that, DLS (Zetasizer, Malvern, Worcestershire, UK) was used to measure the size of aggregated particles, and in this process, 40 µL of samples were injected into a cuvette. Then, the data for each sample were collected through 12~14 scans.

Substrate modification for understanding the interaction between Aβ and AuNPs.

We modified the glass substrate with three types of functional groups which exhibit different charge property. We performed three different types of glass surface modification which are amino-functionalization (positively charged), piranha etching (highly negatively charged), and the glass coated with citrate- modified AuNPs (negatively charged). The coverslips (Fisher Scientific, Pittsburgh, PA, USA) were placed in piranha solution (3:1=concentrated sulfuric acid / 30 % hydrogen peroxide) for 10min to wash out impurities and to produce hydrophilic (negatively charged) property. Firstly, we modified the piranha etched glass with amino functional group using APTMS ((3-Aminopropyl)trimethoxysilane) (Sigma, Saint Louis, MO, USA) to introduce positively charged surface at pH 7.4. The etched substrate was soaked with 2 % APTMS in acetone solvent. To make citrate-modified AuNP (50 nm) coated substrate, amino-functionalized glass was incubated with citrated-AuNPs on account of electrostatic interaction between citrated-AuNPs and amine group on the modified substrate. For negatively charged surface, the piranha etched glass was utilized.[47] We also measured the zeta potential of each modified substrates using the electrophoretic light scattering spectrophotometer (ELS 8000, Otsuka Electronics, Osaka, Japan).

Image Analysis.

To compare the growth rate of Aβ incubation with AuNPs condition to without AuNPs, we performed images analysis using Image Pro Plus program. First, we selected aggregates which have area range from 1 μm^2 to 1000 μm^2 in dark-filed images. Thereafter, we sorted the data in descending numerical order. We selected the 100 objects in results and counted the number of aggregates which were involved in each area range. We calculated the aspect ratio between major axis and minor axis of an ellipse-shaped structure in the dark-field images of 48 hr samples in two different conditions (with AuNPs and without AuNPs). We also obtained the RGB histogram analysis data from the dark-field images using this program.

Circular Dichroism Measurement. To confirm the secondary structure of Aβ aggregates, we used a circular dichroism (CD) spectrometer (Chirascan Plus, AppliedPhotophysics, UK). For obtaining the signal of Aβ *in situ* without disruption the brain SLB structure and Aβ aggregate structures, we fabricated SLB on quartz cell for CD spectrometer. First, quartz cells were soaked in piranha solution (3:1= concentrated sulfuric acid / 30 % hydrogen peroxide) for 20 min, thoroughly rinsed with deionized water, and then dried with a stream of nitrogen. Small unilamellar vesicles (SUV, 100 nm diameter) of 98 mol % brain total lipid extract and 2 mol % NBD-PC were mixed 3:1 (v/v) with phosphate-buffered saline, and 400 μL of the resulting solution was added into a piranha-etched quartz cell. After incubation for 30 min at room temperature, the quartz cell was washed with deionized water and 10 mM phosphate buffer (PB, pH 7.4) to remove excess vesicles and to optimize condition for Aβ growth. Finally, 330 μL of the Aβ solutions was added to the newly formed SLB. Immediately, the sealed-quartz cells were incubated at 37˚C for 0, 24 and 48 hours. We also checked the fluidity of SLB *via* fluorescence recovery after photobleaching method. The secondary structure content was analyzed by CDNN program (AppliedPhtophysics, Leatherhead, Surrey, UK).

2.3. Results and Discussion

2.3.1. AuNP aggregation-based plasmonic color change.

Dark-field light scattering generates different colors with the same AuNPs based on change in the plasmonic coupling between AuNPs.[23-26] First, we set up and validated the plasmonic coupling-based color change of AuNPs. Various amounts of salt were added to AuNPs to induce differently coupled AuNP aggregates. It is well known that higher amount of salt can induce more charge screening effect, larger AuNP aggregates and stronger plasmonic

coupling-based color change.[27, 28] As the size of AuNP aggregates get larger, dark-field light scattering color turns from green to red. This trend was confirmed by the transmission electron microscope (TEM) images (JEOL-JEM 2100, JEOL, Tokyo, Japan), UV-Vis spectrophotometer (Agilent 8453E, Agilent, CA, USA) and dynamic light scattering analysis (Zetasizer, Malvern, Worcestershire, UK), respectively (Figure 2.2a). The color histogram results for each case prove that larger AuNP aggregates generate more reddish and less greenish color in the dark-field images (Figure 2.2a). All these results support that changing in the dark-field color from green to red can be used as a sensitive and reliable measuring stick in monitoring Aβ assembly process.

2.3.2. Aβ aggregation on brain SLB.

In a typical experiment, first, to measure the fluidity of the lipid bilayer [98 mol % brain total lipid extract + 2 mol % NBD-PC (1-oleoyl-2-{6-[(7-nitro-2-1,3-benzoxadiazol-4-yl)amino] hexanoyl}-sn-glycero-3-phosphocholine)], a focal region of the SLB was photobleached and monitored. After 5 min, the recovery of fluorescence signal from the photobleached region was observed via the fluid mixing between lipids in the photobleached and non-photobleached areas, indicative of high lipid mobility in the brain SLB (the inset images in Figure 2.1). Next, we demonstrated that the brain SLB plays significant roles in Aβ aggregation by comparing the Aβ assembly on the brain SLB to the Aβ assembly on the piranha-etched bare glass substrate (48-hr incubation at 37 ℃, pH 7.4; Figure 2b; see the method section for experimental details). For the piranha-etched glass substrate, random aggregates and large bundles with less fibrillar features were observed. On the brain SLB platform, it was clearly seen that many elongated fibrillar structures were formed (Figure 2.2b). A supported membrane can preserve the key properties of a cell membrane, especially

lipid fluidity that can laterally move any modified structures to efficiently form aggregate structures.[29, 30] Aβ has two distinct regions-hydrophobic transmembrane region (amino acid residue 29-42) and hydrophilic extracellular domain (amino acid residue 1-28).[31] The brain total lipid extract-based SLB has weakly negative charges (-7.23 mV) due to the anionic lipid components in the SLB such as phosphatidic acid (PA), phosphatidyl serine (PS), phosphatidyl glycerol (PG) and phosphatidyl inositol (PI). These weakly negative charges on the SLB could offer the electrostatic binding sites to positively charged domain in the charge distribution of Aβ.[32] Furthermore, the self-assembled hydrophobic parts of lipids could interact with the hydrophobic transmembrane region in the Aβ.[27] It should be noted that lipid components can move around to fit into a right configuration for the efficient interactions between lipids and Aβ. For these reasons, the brain SLB could offer both a myriad of binding sites for Aβ and the fluid lipid substrate that readily provides lateral mobility of bound Aβ molecules for a fast and efficient 2-dimensional Aβ assembly. On the other hand, piranha-etched glass surface is negatively charged. At pH 7.4, Aβ has a net negative charge because the pI value of Aβ is 5.2. There are the repulsive forces between piranha-etched glass and Aβ. Further, the binding between the hydrophobic region in Aβ and negatively charged hydrophilic solid surface is energetically unfavorable - flattened globular Aβ aggregate structure was found on anionic hydrophilic mica surface whereas elongated-β sheet Aβ structure was formed on a hydrophobic graphite.[31, 33]

2.3.3. Imaging and characterizing Aβ aggregation process with plasmonic AuNPs.

Next, imaging and characterizing Aβ aggregation process with plasmonic AuNPs were performed. We were able to obtain the structural details of Aβ aggregates with photostable AuNP labels and dark-field microscopy.[21] The green color is mainly attributed to AuNP

scattering, and the scattering color is greener due to the existence of non-coupled AuNP labels.[34] To compare a fluorescence-based image to the dark-field-based image, an immunostaining method was applied to Aβ aggregates on the SLB (Figure 2.2c). For this experiment, anti-Aβ antibody (6E10, Covance, NJ, USA) and Texas-Red-conjugated anti-mouse secondary antibody (ab6726, abcam, Cambridge, UK) were subsequently added for a fluorescence imaging immediately after the deposition of 50-nm citrated-AuNPs (50 pM) for dark-field images. The resulting Aβ aggregates on the brain SLB were imaged with a fluorescence microscope (Carl Zeiss, Germany; 40x objective lens, exposure time: 2 s) and a dark-field condenser (Carl Zeiss, Germany; 40x objective lens, NA=1.4, exposure time: 500 ms), respectively. We obtained the total intensity values from the dark-field and fluorescence images using the intensity histogram analysis function (Image Pro Plus program) (Figure 2.2c). The data show that the photobleaching problem for fluorescence-based imaging method is significant while such a problem does not exist for the AuNP-based dark-field imaging method (Figure 2.2c). This result implies *in situ* quantitative monitoring and data analysis are attainable for the investigation of Aβ fibrillogenesis and plaque-forming processes using plasmonic nanoparticle labels on a SLB platform. It is known that fibrillar structures can be imaged using the dark-field microscopic method without any labels,[35] and we can assume that the scattering signals are from both Aβ aggregate structures themselves and labeled AuNPs. However, without AuNP labels, significantly less features and details were imaged and some parts are even missing in the image (data not shown).

To confirm the interaction between Aβ and AuNP, the Bradford assay for unbound Aβ peptides after incubation with various substrates [(3-aminopropyl) trimethoxysilane (APTMS)-modified surface (positive charge), piranha-etched glass surface (negative charge), and citrate-AuNP-modified surface (negative charge)] was performed, and the zeta potentials

32

were measured to estimate their surface charges. The results show that Aβ peptides have a high affinity to poitively charged APTMS-glass surface while the lower affinity from Aβ peptides was observed for negatively charged piranha-etched glass surface due to strong repulsive forces. Most importantly, Aβ peptides interacted with negatively charged citrate-AuNP-modified surface as effectively as positively charged glass-APTMS surface. The results indicate that the citrates on AuNP surface do not directly interact with the peptides but are readily exchanged by Aβ peptides for the formation of AuNP-Aβ complexes. In other words, AuNPs were directly attached to Aβ peptides (pI value = 5.2) via the electrostatic interactions at pH 7.4.[36]

2.3.4. The roles of AuNPs for Aβ aggregation on brain SLB.

To observe the roles of AuNPs for Aβ aggregation on brain SLB, first, Aβ peptides were aggregated on the brain SLB substrate in the absence of AuNPs, and AuNPs were then labeled to Aβ aggregates immediately before the dark-field imaging (Figure 2.3a). As shown in Figure 3a, it took ~4-8 hrs to form protofibrils, and the elongated and entangled fibril features became clear after 12-hr incubation. After 24-hr incubation, long Aβ fibrils were formed, and fibril bundles were observed after 48-hr incubation. Overall, a dominant dark-field color was green from 4 to 48 hr incubation, suggesting Aβ fibrils were mostly formed and organized with a regular interlayer distance between β-sheet layers. There were no distinct cores in these aggregates. Next, we investigated the effect of AuNPs on Aβ aggregation and large plaque structure formation (Figure 2.3b). It was reported that the nucleation of protein fibrillation can be stimulated by nanoparticles due to the enormous surface-to-volume ratio, offered by nanoparticles, and protein structure can be altered by the interaction between proteins and nanoparticles.[24] Moreover, a high local protein

concentration (e.g., the formation of multiple protein layers on nanoparticle surface) can result in a shortened lag-time for Aβ assembly, and protein aggregation and fibrillation are highly dependent on protein type and concentration as well as nanoparticle type and concentation.[43, 44] In our case, we observed >10-nm-thick Aβ layer was formed on an AuNP surface within 20 min (dynamic light scattering analysis). We anticipated that these highly localized Aβs on the surface of AuNPs can stimulate and alter the Aβ assembly process.

In a typical experiment, soluble Aβ peptides (20 μM in 10 mM phosphate buffer solution at pH 7.4) and 50-nm AuNPs (50 pM in 10 mM phosphate buffer solution at pH 7.4) were mixed together. The mixture was injected into the brain SLB-modified chamber or a glass chamber (slide glass chamber, Live Cell Instrument, South Korea) and incubated at 37 ˚C for 48 hr (Figure 2.3b). After 2-4 hr incubation, unlike the above case with no AuNPs, many small aggregates with no observable fibrillar feature were formed and green dark-field scattering color was observed from the aggregated structures. At 8-hr incubation, Aβ peptides were not assembled to form fibrils but aggregated into a globular or amorphous form with AuNPs were densely aggregated with Aβ peptides as the strong plasmonic inter-particle coupling color (red) and image size suggest (Figure 2.3b). The red-colored Aβ-AuNP aggregates can serve as a nucleus for the formation of large Aβ aggregate structures. After 12 hr incubation, more Aβ aggregates with red and yellow scattering color were formed, and the yellowish scattering color suggests the formation of the additional outer Aβ-AuNP layer on a dense Aβ-AuNP aggregate core. As the incubation time was increased to 24 hrs, aggregate structures get larger, and yellowish peripheral Aβ-AuNP structures on a red Aβ-AuNP core were clearly observed. At 48 hr incubation, large Aβ plaque-like structures with densely structured red cores and more yellowish peripheral features (~20 μm in diameter) were formed (Figure 2.3b). The results show that, rather than forming fibrillar structures,

amorphous Aβ aggregate structures with a dense Aβ-AuNP core can be formed with AuNPs on the brain SLB without going through fibrillar structures. To examine the correlation between Aβ aggregate structures and AuNPs, Aβ-AuNP aggregates were labeled with fluorophores via Aβ immunostaining (see the Method section for experimental details) on the brain SLB. First, the AuNPs in Aβ-AuNP aggregates were dissolved by 350 mM KCN after 12 hr incubation to confirm AuNPs were densely incorporated in Aβ aggregate. The color of Aβ-AuNP aggregates disappeared or was changed from reddish orange to bluish white after dissolving AuNPs with KCN, indicative of the removal of AuNPs in Aβ aggregates. The result proves that AuNPs were incorporated throughout Aβ aggregates, and these particles are responsible for the generation of reddish dark-field color. After 48-hr incubation, the aggregates were labeled with fluorophores and imaged with a fluorescence microscope and the dark-field light scattering method, respectively (Figure 2.4a). The results show the fluorescence signal intensity from the Aβ structure was uniformly distributed throughout an Aβ plaque-like structure without any core feature while AuNPs were densely located in the core area of Aβ plaque-like structures. It is known that breaking hydrogen bonds or exciting bending or stretching modes within cross-β core structures can induce the fragmentation or alteration of an Aβ aggregate structure[45] and weaken fibrillar structures.[46] AuNPs can interrupt the interactions within cross-β core structure and alter organization of β-sheet structures. We also obtained the TEM images of Aβ aggregate structures (Figure 2.4b). In the case of Aβ incubation without AuNPs, fibril structures were dominantly formed. On the other hand, when Aβ was co-incubated with AuNPs, large amorphous AuNP-Aβ co-aggregate structures were observed with nearly no fibrillar features (please see the experimental section for experimental details). The results suggest that nanoparticles can be used as the core platform structure for Aβ aggregation, and further Aβ structure assembly can be altered and tuned on this platform to form a large Aβ aggregates.[47]

For protein fibrillation, the high surface area of AuNPs, coupled with the dynamic exchange of proteins between bound or free forms, may lead to a high local concentration of Aβ on nanoparticle surface and may facilitate oligomer formation via a shortened lag-time for Aβ assembly.[48]

2.3.5. Quantitative and structural analysis of Aβ-AuNP co-aggregates on brain SLB.

From the dark-field color histogram results for green and red colors, we could quantitatively analyze inter-particle couplings (Figures 2.5a and 2.5b). For Aβ incubation without AuNPs on the brain SLB (AuNPs were added later only for the purpose of imaging in this case), green color increased linearly as incubation time increased while increase in red color is little or negligible as a function of incubation time (Figure 2.5a). This shows that the number of modified AuNPs increased as incubation time was increased, but Aβ-AuNPs are not densely incorporated in this case. In the case that Aβ peptides were co-incubated with AuNPs on the brain SLB, the intensities in both green and red colors increased after 24-hr incubation. Significant increase in red color indicates the existence of closely spaced AuNPs in the Aβ aggregate structures. Importantly, there is a steep increase in the color intensity from 12-hr to 24-hr incubation time for both green and red colors, and this shows that there is increase in both the number of AuNPs and more couplings between AuNPs in forming larger Aβ aggregates from this time frame (Figure 2.5b). These further suggest that plaque-like Aβ structures did not go through gradual growth of fibrillar structures when AuNPs were co-incubated. The dark-field images of 24-hr and 48-hr incubations were then analyzed using the Image-Pro Plus program. We measured the area, ranging from 1 μm^2 to 1000 μm^2, and calculated the average area and aspect ratio of each Aβ aggregate. The average size of aggregated Aβ structures for each condition was measured and obtained (Figure 2.5c). The

results clearly showed that the co-incubation of Aβ peptides with AuNPs on the brain SLB generated larger Aβ aggregates than the cases without AuNPs on the brain SLB. Further, the aspect ratio of Aβ aggregate structures was studied. We calculated the aspect ratio of 100 Aβ aggregates for each condition after 48-hr incubation from the dark-field scattering image analysis. The co-incubation with AuNPs on the brain SLB generates more globular aggregate structures than the condition without AuNPs on the brain SLB (Figure 2.5d). All these results further suggest that both AuNP seeds and brain SLB play important roles in altering Aβ assembly process and inducing very large Aβ aggregate structures.

To fully grasp change in Aβ structures, the detailed analysis of the secondary structures of proteins is critical. It is known that β-sheet structures are rich in both amyloid fibrillar and plaque structures.[11] To study the role of β-sheet structures and other secondary structures in forming Aβ aggregates with AuNPs on the brain SLB, we simultaneously used the dark-field imaging and circular dichroism (CD) spectrometer to confirm the richness of β-sheet secondary structures and other structural features in Aβ aggregates with and without AuNPs for 24-hr and 48-hr incubation cases on the brain SLB (Figure 2.6a). To obtain the *in situ* data from Aβ aggregate structures on the brain SLB without disrupting the structures during the sampling process, we fabricated the brain SLB directly on a quartz cell surface for the CD spectrometer measurement and the dark-field imaging (Figure 2.6; see the Method for the experimental procedures). After 48-hr incubation, the dark-field image and CD results clearly showed that the fibrillar structures with more β-sheet features (mainly β-strand) were found when no AuNPs were added. When compared to the case with no brain SLB and no AuNPs, dramatic decrease in random coil feature and increase in α-helix feature were also observed in this case. In the case with AuNPs on the brain SLB, when compared to the case with no AuNPs on the brain SLB, α-helix and β-strand features were decreased while random

coil features were remarkably increased (Figure 2.6c and 2.6d). The results suggest that AuNPs boost the formation of random coil features and could hinder the unfolding of oligomer units for the formation of twisted fibrillar[49] or non-fibrillar structures. Surface-bound Aβ has less degree of freedom including translational protein folding and rotational freedom than free Aβ in solution. It is known that the folding of chains into amorphous aggregates that are in dynamic equilibrium is common whereas it is unlikely for chains to fold into ordered β-sheet-rich structures.[50, 51] For these reasons, the amorphous structures with less β-sheet features were formed and more random coils structures were formed when Aβ was co-incubated with AuNPs on the brain SLB. However, the results also indicate that β-sheet structures still play roles in forming larger plaque-like structures. Based on all the observations, the brain SLB enriches secondary structures (both α-helix and β-sheet) and Aβ binding to AuNPs induces more random coil structures while reducing α-helix and β-sheet features in large Aβ aggregates (e.g., Aβ plaques). Further, nanoparticles can decrease the lag time for nucleation and offer many nucleation sites and large nucleation surface for an efficient Aβ peptides.

2.4. Conclusion

We showed the roles of the brain SLB and AuNPs in forming large Aβ aggregates, and it is clear that the brain SLB facilitates fast and efficient formation of Aβ aggregates and AuNPs can alter secondary protein structures in Aβ. By inducing Aβ aggregation with these two substrates simultaneously, large Aβ plaque structures (>15 μm in diameter) were formed within a short incubation time without going through fibril structures that are typically found

in a majority of other Aβ aggregation processes. The dark-field scattering and circular dichroism-correlation results indicate that AuNPs were heavily involved with Aβ aggregation, especially in the core part, and the structural features with less α-helix, less β-sheet and more random coil structures were induced due to the presence of both AuNPs on the brain SLB. We also show that AuNPs can also be used as photostable imaging probes for the *in situ* analysis of the involvement of AuNPs in forming Aβ aggregates and the structural details of Aβ aggregates. The use of AuNPs as imaging labels is highly beneficial because AuNPs are photostable labels and we do not need to further modify Aβ aggregates with additional imaging labels. Our strategy offers many analytical details with flexibility in adopting many components within a brain-mimicking environment and can offer a new platform for the mechanistic and structural studies of Aβ aggregate-related diseases and drug screening assays for AD. Further, this approach could be readily applied to study other protein aggregation-related systems such as prions for the Mad Cow disease and α-synucleins for the Parkinson's disease. Finally, we envisage this platform can be used to study the roles of various nanostructures in protein aggregations for finding new functions of nanoparticles in AD and the better understanding, diagnosis and cure of AD and other protein aggregation-related diseases. To test its potential for *in vivo* applications, although it has been shown different Aβ aggregates have different effects on AD, the effects of various AuNP-Aβ aggregates on neuronal cells and brain need to be studied further. It should be also noted that our strategy and platform offer insight in material design and synthesis and can also be useful for the fabrication of many new types of nanostructures and biomaterials.

2.5. References

1. J. Hardy, D. J. Selkoe, *Science* **2002**, 297, 353.

2. F. Mangialasche, A. Solomon, B. Winblad, P. Mecocci, M. Kivipelto, *Lancet Neurol.* **2010**, 9, 702.

3. S. L. Bernstein, N. F. Dupuis, N. D. Lazo, T. Wyttenbach, M. M. Condron, G. Bitan, D. B. Teplow, J.-E. Shea, B. T. Ruotolo, C. V. Robinson, M. T. Bowers, *Nat. Chem.* **2009**, 1, 326.

4. C. Soto, *Nat. Rev. Neurosci.* **2003**, 4, 49.

5. W. B. Stine, K. N. Dahlgren, G. A. Krafft, M. J. LaDu, *J. Biol. Chem.* **2003**, 278, 11612.

6. N. Arispe, M. Doh, *FASEB J.* **2002**, 16, 1526.

7. M. Katsumi, *BBA –Biomembr.* **2007**, 1768, 1935.

8. M. J. Kogan, N. G. Bastus, R. Amigo, D. Grillo-Bosch, E. Araya, A. Turiel, A. Labarta, E. Giralt, V. F. Punte, *Nano Lett.* **2006**, 6, 110.

9. D. Zhang, O. Neumann, H. Wang, V. M. Yuwono, A. Barhoumi, M. Perham, J. D. Hartgerink, P. Wittung-Stafshede, N. J. Halas, *Nano Lett.* **2009**, 9, 666.

10. E. P. O'Brien, J. E. Straub, B. R. Brooks, D. Thirumalai, *J. Phys. Chem. Lett.* **2011**, 2, 1171.

11. T. P. J. Knowles, M. J. Buehler, *Nat. Nanotech.* **2011**, 6, 469.

12. M. Li, C. Xi, Li Wu, J. Ren, E. Wang, and X. Qu, *Small* **2013**, 9, 3455.

13. M. Li, X. Yang, J. Ren, K. Qu, and X. Qu, *Adv. Mater.* **2012**, 24, 1722.

14. D. Brambilla, R. Verpillot, B. Le Droumaguet, J. Nicolas, M. Taverna, J. Kóňa, B. Lettiero, S. H. Hashemi, L. De Kimpe, M. Canovi, M. Gobbi, V. Nicolas, W. Scheper,

S. M. Moghimi, I. Tvaroška, P. Couvreur, K. Andrieux, *ACS Nano* **2012**, 6, 5897.

15. D. Brambilla, R. Verpillot, M. Taverna, L. D. Kimpe, B. L. Droumaguet, J. Nicolas, F. Mantegazza, M. Canovi, M. Gobbi, M. Salmona, V. Nicolas, W. Scheper, P. Couvreur, K. Andrieux, *Anal. Chem.* **2010**, 82, 10083.

16. D. Brambilla, B. L. Droumaguet, J. Nicolas, S. H. Hashemi, L. P. Wu, S. M. Moghimi, P. Couvreur, K. Andrieux, *Nanomedicine: Nanotechnology, Biology, and Medicine* **2011**, 7, 521.

17. W. E. Doering, S. Nie, *J. Phys. Chem.* B. **2001**, 106, 311.

18. C. Loo, L. Hirsch, M-H. Lee, E. Chang, J. West, N. J Halas, R. Drezek, *Opt. Lett.* **2005**, 30, 1012.

19. A. Aguzzi, T. O'Connor, *Nat. Rev. Drug Discov.* **2010**, 9, 237.

20. C. Pike, D. Burdick, A. Walencewicz, C. Glabe, C. Cotman, *J. Neurosci.* **1993**, 13, 1676.

21. F. Chiti, C.M. Dobson, *Annu. Rev. Biochem.* **2006**, 75, 333.

22. Y. Gong, Y, L. Chang, K .L. Viola, P. N. Lacor, M. P. Lambert, C. E. Finch, G. A. Krafft, W. L. Klein, *Proc. Natl. Acad. Sci. U.S.A.* **2003**, 100, 10417.

23. D. A. White, A. K. Buell, C. M. Dobson, M. E. Welland, T. P. J. Knowles, *FEBS Lett.* **2009**, 583, 2587.

24. M. P. Matton, *Nature* **2004**, 430, 631.

25. A. Nazem, G. A. Mansoori, *J. Alzheimer's Disease* **2008**, 13, 199.

26. K. Salaita, P. M. Nair, R .S. Petit, R. M. Neve, D. Das, J. W. Gray, J. T. Groves, *Science*

2010, 327, 1380.

27. Y.-H. M. Chan, S. G. Boxer, *Curr. Op. Chem. Biology.* **2007**, 11, 581.

28. S. Linse, C. Cabaleiro-Lago, W-F. Xue, I. Lynch, S. Lindman, E. Thulin, S. E. Radford, K. A. Dawson, *Proc. Natl. Acad. Sci. U.S.A* **2007**, 104, 8691.

29. C. Sonnichsen, B. M. Reinhard, J. Liphardt, A. P. Alivisatos, *Nat. Biotech.* **2005**, 23, 741.

30. J. Yguerabide, E. E. Yguerabide, *Anal. Biochem.* **1998**, 262, 157.

31. J. N. Anker, W. P. Hall, O. Lyandres, N. C. Shah, J. Zhao, R. P. Vandyne, *Nat. Mater.* **2008**, 7, 442.

32. G. Raschke, S. Kowarik, T. Franzl, C. Sonnichsen, T. A. Klar, J. Feldmann, A. Nichtl, K. Kurzinger, *Nano Lett.* **2003**, 3, 935

33. C. D. Keating, M. D. Musick, M. H. Keefe, M. J. Natan, *J. Chem. Educ.* **1999**, 76, 949.

34. R. Jin, *Angew. Chem. Int. Ed.* **2010**, 49, 2826.

35. K. D. Mossman, G. Campi, J. T. Groves, M. L. Dustin, *Science* **2005**, 310, 1191.

36. M. B. Forstner, C. K. Yee, A. N. Parikh, J. T. Groves, *J. Am. Chem. Soc.* **2006**, 128, 15221.

37. T. Kowalewski, D. M. Holtzman, *Proc. Natl. Acad. Sci. U.S.A.* **1999**, 96, 3688.

38. B. Bonev, A. Watts, M. Bokvist, G. Gro¨bner, *Phys. Chem. Chem. Phys.* **2001**, 3, 2904.

39. M. Bokvist, F. Lindstro¨m, A. Watts, G. Gro¨bner, *J. Mol. Biol.* **2004**, 335, 1039.

40. N. L. Rosi, C. A. Mirkin, *Chem. Rev.* **2005**, 105, 1547.

41. Y. Choi, S. Hong, T. Kang, L. P. Lee, *J. Phys. Chem. C* **2009**, 113, 14587.

42. K. Yokoyama, D. R. Welchons, *Nanotechnology* **2007**, 18, 105101.

43. A. E. Nel, L. Madler, D. Velegol, T. Xia, E. M. Hoek, P. Somasundaran, F. Klaessig, V. Castranova, M. Thompson, *Nat. Mater.* **2009**, 8, 543.

44. S. C. Wagner, M. Poskamp, M. Pallerla, R. R. Araghi, S. Schlecht, B. Koksch, *Small* **2010**, 6, 1321.

45. R. Paparcone, M. J. Buehler, *Biomaterials* **2011**, 32, 3367.

46. J. Shorter, S. Lindquist, *Molecular Cell* **2006**, 23, 425.

47. V. L. Colvin, K. M. Kulinowski, *Proc. Natl. Acad. Sci. U.S.A* **2007**, 104, 8679.

48. L. Fei, S. Perrett, *Int. J. Mol. Sci* **2009**, 10, 646.

49. B. Moores, E. Drolle, S.J. Attwood, J. Simons, Z. Leonenko, *PLoS ONE* **2011**, 6, e25954.

50. A. K. Paravastu, R. D. Leapman, W.-M. Yau, R. Tycko, *Proc. Natl. Acad. Sci. U.S.A* **2008**, 105, 18349.

51. G. Boucher, N. Mousseau, P. Derreumaux, *Proteins: Struct. Funct. Bioinf.* **2006**, 65, 877.

52. S. C. Hayden, G. Zhao, K. Saha, R. L. Phillips, X. Li, O.R. Miranda, V. M. Rotello, M. A. El-Sayed, I. Schmidt-Krey, U. H. F. Bunz, *J. Am. Chem. Soc.* **2012**, 134, 6920.

53. K. J. Seu, A. P. Pandey, F. Haque, E. A. Proctor, A. E. Ribbe, J. S. Hovis, *Biophys. J.* **2007**, 92, 2445.
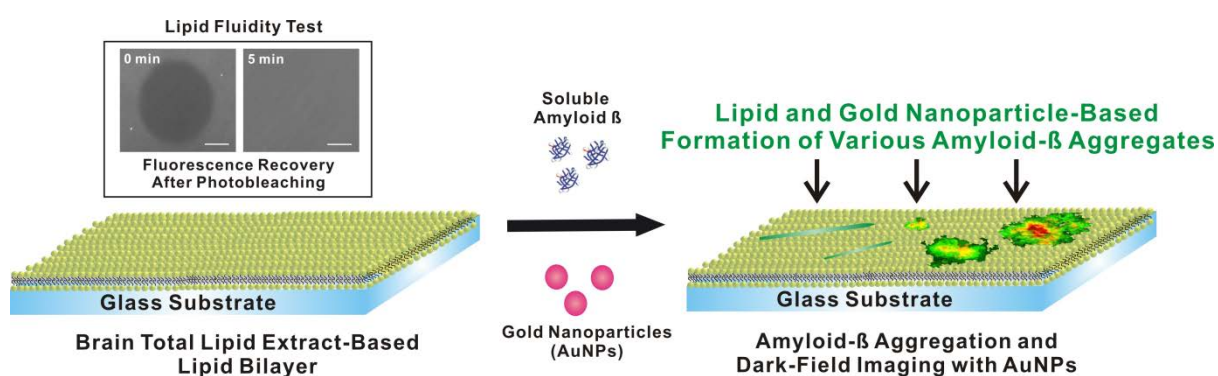
Figure 2.1. Schematic illustration of Au nanoparticle-based Aβ aggregation and imaging assay on brain lipid bilayer. Au nanoparticles were used as both Aβ aggregation seeds and photostable imaging probes. The inset figures on the upper left are the fluorescence recovery after photobleaching images to confirm the fluidity of the brain SLB. Scale bar is 10 μm for the images.
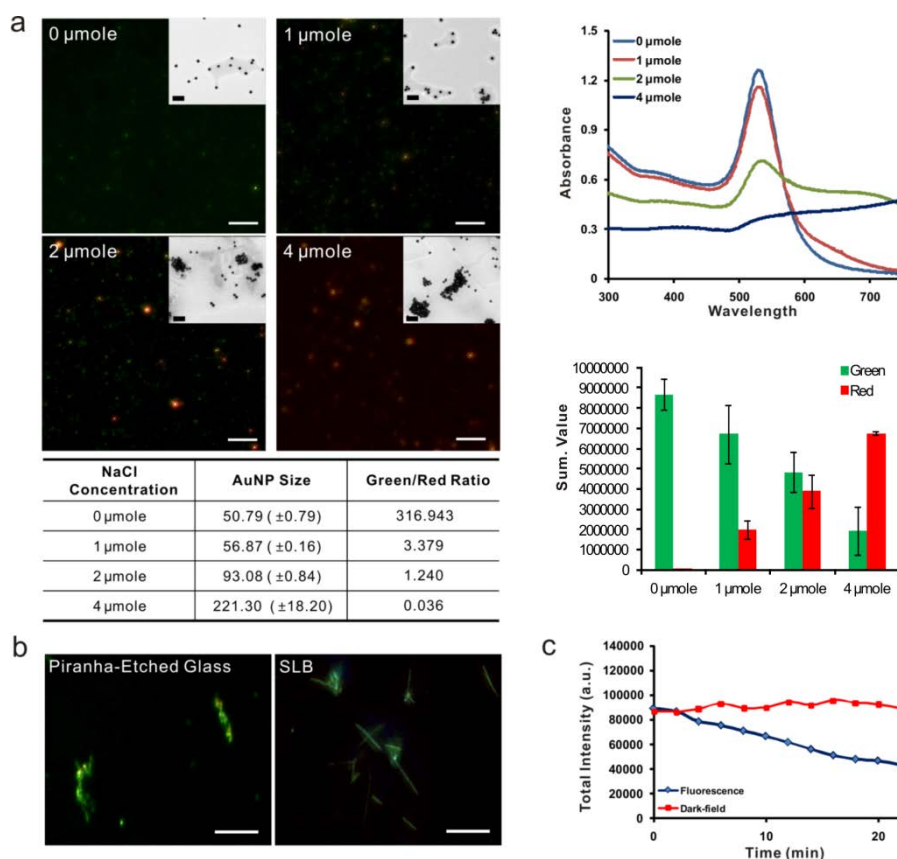
NaCl Concentration	AuNP Size	Green/Red Ratio
0 µmole	50.79 (±0.79)	316.943
1 µmole	56.87 (±0.16)	3.379
2 µmole	93.08 (±0.84)	1.240
4 µmole	221.30 (±18.20)	0.036

Figure 2.2. AuNP aggregation and dark-field imaging analysis. (a) The surface plasmon band of aggregated AuNPs was red-shifted (red color in the dark-field image), compared to non-aggregated AuNPs (green color in the dark-field image, scale bar = 10 µm). Increase in salt concentration induces more nanoparticle aggregations (TEM images, scale bar = 200 nm). The dynamic light scattering and UV-Vis data further support inter-nanoparticle-coupling-based optical signal change. Color histogram graph shows the sum values of green and red colors in each salt concentration (please notice that the total sum value is same in every case). The green-to-red ratio is highest when there is no salt. (b) Comparison between piranha-etched glass and brain total lipid extract-based SLB as an Aβ aggregation platform. The images were obtained after 24-hr Aβ incubation at 37 °C. Scale bar is 20 µm for all the images. (c) The real-time optical signal tracking of fluorescent and dark-field images.
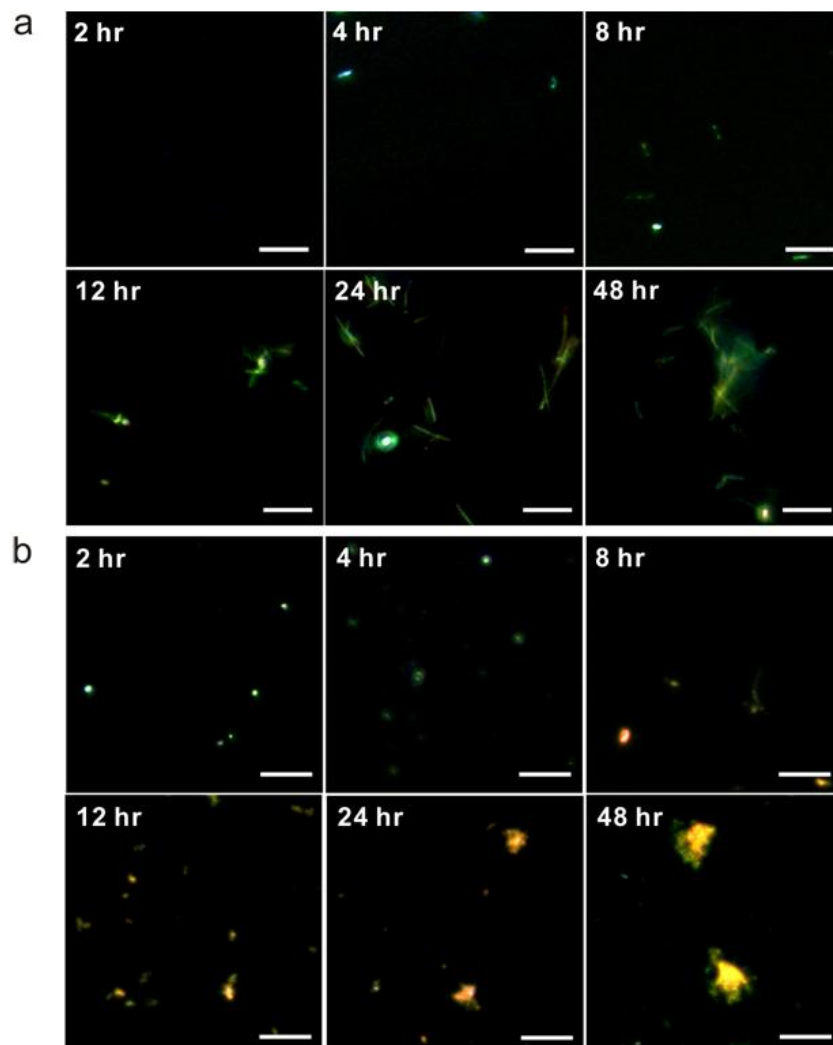
Figure 2.3. The time-lapse dark-field images of Aβ aggregates without and with AuNPs (a and b, respectively) on the brain SLB . Scale bars in all the images are 20 μm.
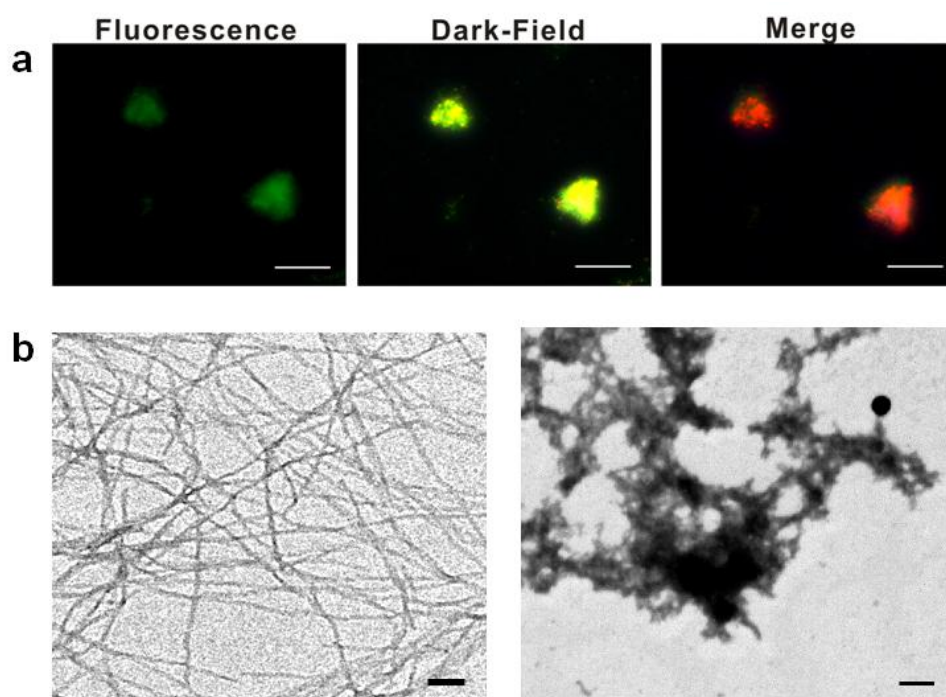
Figure 2.4. Optical and TEM image analysis on AuNP-Aβ aggregates. (a) Fluorescence-dark-field overlap images of plaque-like large Aβ aggregates. Fluorophore-labeled Aβ was incubated with AuNPs. Scale bars in the images are 20 µm. (b) TEM images of Aβ aggregates without AuNPs (left) and with AuNPs (right). Scale bars in both images are 100 nm. Incubation time is 48 hr for all the images.
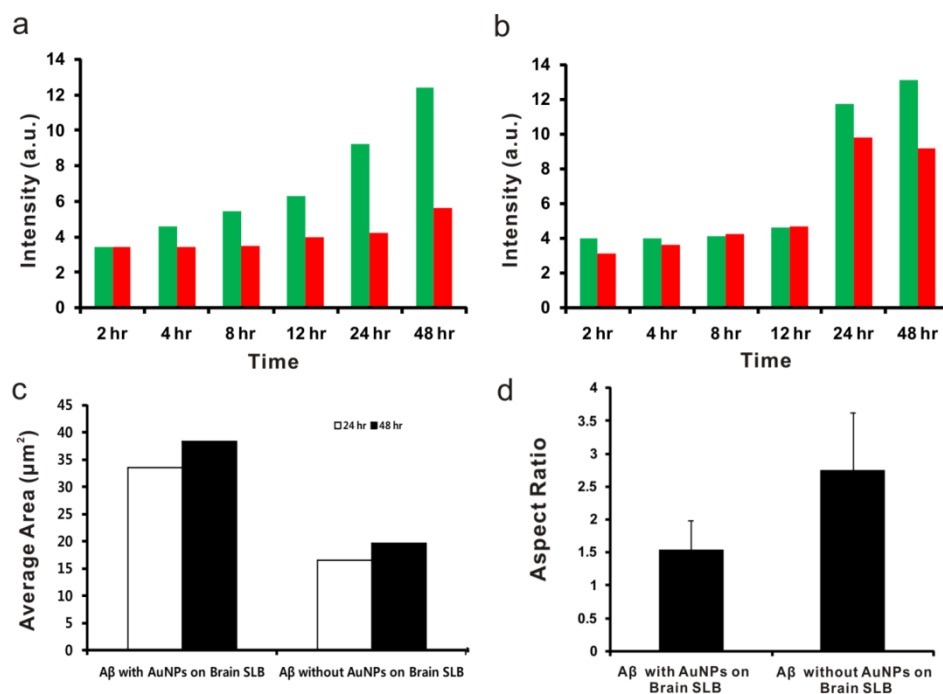
Figure 2.5. The dark-field color, size and shape analysis of Aβ aggregates on the brain SLB. (a) Dark-field-based green and red color histogram for Aβ aggregates without AuNPs on the brain SLB. (b) Dark-field-based green and red color histogram for Aβ aggregates with AuNPs on the brain SLB. (c) Aβ size analysis after 24 hr and 48 hr incubation. ~100 Aβ aggregates were analyzed for each case (only average size values are shown). (d) The aspect ratio of Aβ aggregates in the dark-field images after 48 hr incubation.
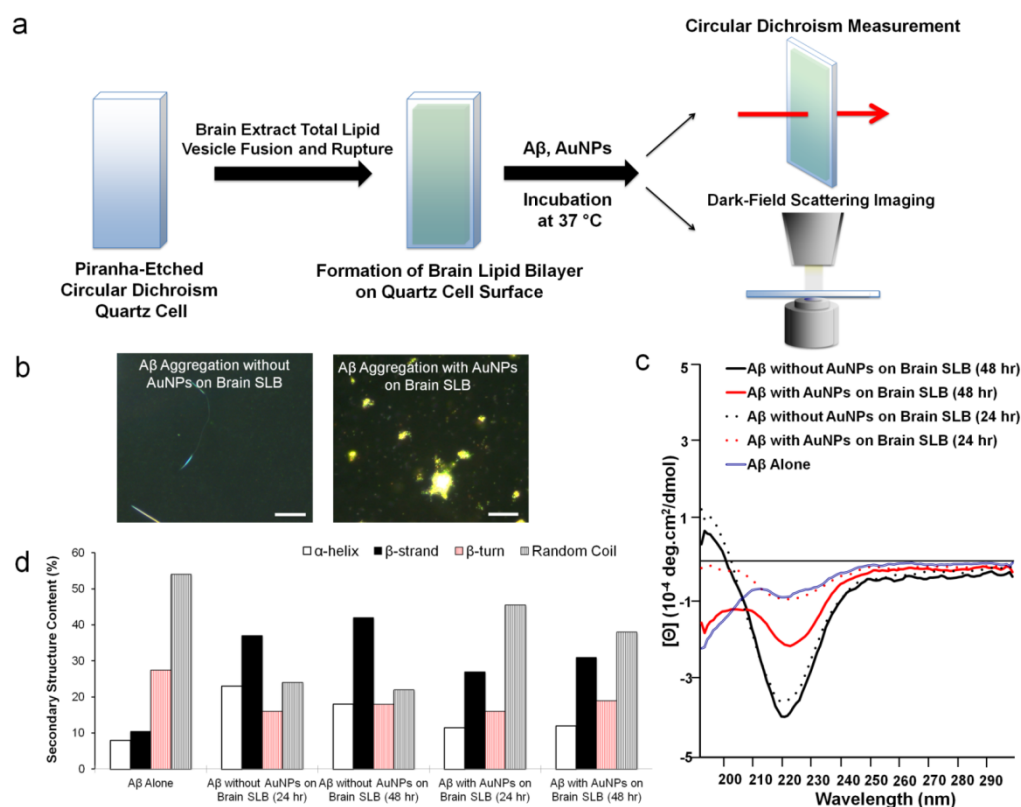
Figure 2.6. The circular-dichroism-dark-field correlation measurements and the secondary structure analysis on Aβ aggregates. (a) The schematic diagram of the circular dichroism (CD) and dark-field co-analysis using a quartz cell. (b) The dark-field images of Aβ aggregates on the brain SLB that was formed on a quartz cell surface after 48 hr incubation. The scale bars in all images are 20 μm. (c) The CD results after 24 and 48 hr incubation for the condition with and without AuNPs. Three replicate experiments were repeated for each case. (d) The secondary structure analysis on Aβ aggregates with the CD data.

Chapter 3. How Do the Size, Charge, and Shape of Nanoparticles Affect Amyloid β Aggregation on Brain Lipid Bilayer?

3.1. Introduction

Alzheimer's disease (AD) is a neurodegenerative disorder; one of its pathogenic features is formation of amyloid beta (Aβ) aggregates, including amyloid plaques and neurofibrillary tangles (NFTs).[1] Aβ is derived from amyloid precursor protein (APP) within the brain membrane; non-toxic Aβ can undergo structural conversion and form various toxic Aβ aggregates that are rich in β-sheet structures.[2, 3] It is widely accepted that Aβ self-assembly is determined by its intrinsic primary sequence properties and alteration of the biological environment plays a key role in Aβ folding and accumulation.[4] Therefore, numerous studies have been conducted on the interactions between lipid membranes and Aβ and the effects of the cell membrane on Aβ aggregation.[5-8] Although it is important to investigate the mechanism of lipid membrane-mediated Aβ aggregation, few properly designed platform-based studies have been published. Recently, we used a total brain lipid extract-based supported lipid bilayer (brain SLB) platform to study Aβ aggregation, using gold nanoparticles (AuNPs).[9] We used AuNPs for *in situ* monitoring of AuNP-Aβ aggregated structures using dark-field microscopy.[9,10] The results implied that the kinetics and mechanism of Aβ fibrillization can be altered by controlling the nucleation process with AuNPs. The addition of nucleation seeds were found to attenuate the lag phase of Aβ fibrillization, which inspired numerous attempts to study and control the influence of nanomaterial nucleation seeds on that process.[11-14] Researchers have also investigated the interaction between Aβ and nanoparticles, using engineered nanoparticles for controlling Aβ

aggregation and curing amyloid-related diseases.[15] It is known that multiple factors control Aβ fibrillization, including the composition and concentration of nanoparticles[11,12] and their surface characteristics.[13,14] Nanoparticles can act not only as nucleation seeds for Aβ growth, with a shorter lag phase and faster growth kinetics, but also as inhibitors of Aβ fibrillization, depending on their physical and chemical properties. However, how the characteristics of nanoparticles, such as particle size, shape, and surface charge, affect the complicated interactions between nanoparticles, Aβ, and the brain SLB have not yet been systematically investigated. This understanding could greatly increase our knowledge of Aβ aggregation in the presence of nanoparticles and facilitate nanoparticle and lipid-based applications in diagnosing and curing Alzheimer's disease and other protein aggregation-related diseases.

3.2. Experimental Section

Procedures for initial preparation of Aβ peptides and preparation of lipid vesicles and the supported lipid bilayer (SLB) were described in a previous paper.[9]

Co-incubation of Aβ with AuNPs and dark-field imaging of Aβ aggregates.

The dark-field chambers containing SLB were washed with 600 μL of 10 mM PB (pH 7.4) by flowing through the space between two glasses to optimize conditions for Aβ fibril growth. AuNPs (10 μL) was mixed with 100 μL of Aβ solution just before use. The AuNP concentrations were varied in accordance with the surface area of each particle. Subsequently, 110 μL of the resulting solution was injected into the chamber, and the samples were incubated at 37°C and 5.0% CO_2 for 6 hr and 48 hr, respectively. Dark-field microscopy was

performed using a 200 inverted microscope (Carl Zeiss, Oberkochen, Germany) equipped with a dark-field condenser (NA = 1.4, oil immersion) and white light illumination from a 100-W halogen lamp. Images were captures using a 40X objective lens (NA = 0.8) (Axiovert 200M, Carl Zeiss, Oberkochen, Germany).

TEM imaging of Aβ aggregates via negative staining.

To prepare TEM specimens, air was injected though the chamber inlet and the solution was then pushed out through the chamber outlet. 10 μL of this solution was dropped onto a TEM grid and after 10 min, the remaining solution was soaked up from the edge of the grid using filter paper. This sample was dried at room temperature overnight before imaging. The specimen was then stained with 10 μL of 2% uranyl acetate solution in deionized water for 1 min, and the staining solution was drawn away from the edge of the grid with a filter paper. The TEM grid was washed with 10 μL of deionized water 3 times and dried overnight at room temperature. Then, we observed the sample using the transmission electron microscope (JEOL-JEM 2100, JEOL, Tokyo, Japan) in the National Center for Inter-University Research Facilities (NCIRF).

Circular dichroism measurement.

We used a circular dichroism (CD) spectrometer (Chirascan Plus, Applied Photophysics, UK) to detect secondary structural changes in Aβ aggregates. To obtain the signal of Aβ aggregates *in situ* without disruption of the brain SLB and Aβ aggregate structures, SLB was fabricated on quartz cells. First, quartz cells were immersed in piranha-etching solution (3:1 = concentrated sulfuric acid / 30% hydrogen peroxide) for 40 min, thoroughly rinsed with deionized water, and then dried with a stream of nitrogen. Small unilamellar vesicles (SUV, 100-nm diameter) of 100 mol% brain total lipid extract were mixed with 150 mM PBS (1:1

(v/v)), and 400 µL of the resulting solution was added into a piranha-etched quartz cell. After 30 min of incubation at room temperature, the quartz cell was washed with 10 mM PB (pH 7.4) to remove excess vesicles and to provide appropriate conditions for Aβ growth. Finally, 400 µL of the Aβ solutions including AuNPs were carefully injected into the quartz cells. The quartz cells were immediately sealed and incubated at 37°C and 5.0% CO_2 for 6 hr and 48 hr. The secondary structure was analyzed using the program CDNN (Applied Photophysics, Leatherhead, Surrey, UK).

Surface-enhanced Raman scattering (SERS) measurement of Aβ-attached AuNPs. Silicon sticker chambers (2.5 mm in diameter) were fixed to 25 mm × 25 mm microscopic cover glasses (Fisher Scientific, Pittsburgh, PA, USA). 10µl of SUV solution (1 mg/ml lipid concentration in PBS) was injected into each chamber and the chambers were incubated for 40 min. Then, the coverglasses were immersed in a deionized water bath and excess SUV suspension was removed with flowing water. Then, the glasses were placed on a Petri dish, and the water level was adjusted to match the height of the sticker chamber. Co-incubated samples of Aβ peptides and AuNPs were prepared immediately before SERS measurements were taken; the concentration was identical to that used for the dark-field and TEM measurements. Lastly, 3 µl of solution was removed from each chamber and 3 µl of the mixed solution of Aβ and AuNPs was injected. SERS signals were obtained after 2 hr, 4 hr, and 6 hr of incubation using a Renishaw inVia microscope equipped with a Leica microscope and the Renishaw WiRE 3.1 software. A 633-nm laser (HeNe laser, 10 mW) was used to produce Raman scattering under a 50X objective lens (N/A = 0.75) with a 10-sec data acquisition period.

Cell viability assay.

SH-SY5Y cells were purchased from the Korean Cell Line Bank (KCLB, Seoul, South Korea)

53

and cultured in 10% fetal bovine serum (FBS)-supplemented Minimum Essential Media (MEM) (Gibco, USA) with 100 U/ml penicillin–100 μg/ml streptomycin (Gibco, USA) at 37°C and 5% CO_2. SH-SY5Y cells were plated at a concentration of 1.0×10^4 cells/well in 96-well plates with 100 μL of media and incubated overnight. Aβ monomers (25 μM) were incubated on SLB with seven different types of gold nanostructures with identical total surface areas, as descried above. A sample containing 25 μM of Aβ monomers without Au nanostructures was also incubated for 6 hr and 48 hr as a control. Then, each specimen was collected by peeling it off the SLB and centrifugation of the resulting solution for 1 min. 10 μL of collected Aβ aggregates was placed onto each well of the 96-well plate, and the samples were incubated for 8 hr at 37°C and 5% CO_2. To test the cytotoxicity of Aβ aggregates to neuroblastoma cells, we used a CCK-8 assay kit (Dojindo Molecular Technologies, Inc., Rockville, MD, USA). After incubation of Aβ aggregates with SH-SY5Y cells, 10 μL of CCK-8 solution was added to each well and absorbance at 450 nm was measured after 1 hr of incubation using a Synergy™ MX (BioTek Instruments, Inc., Winooski, VT, USA).

3.3. Results and Discussion

We studied the effect of changes in nanoparticle size, shape, and surface charge on Aβ aggregation on a brain SLB, using AuNPs with the identical total surface area to exclude the effect of particle surface area as illustrated in Figure 3.1. The dark-field microscopy, Raman spectroscopy, circular dichroism spectroscopy (CD), and transmission electron microscopy (TEM) data were used as analytical tools in this study.

3.3.1. Aβ incubation on the brain SLB.

The SLB was prepared with 100 mol% brain total lipid extract (Avanti, Alabaster, AL, USA) including neutral and anionic lipids. Aβ can bind to anionic lipids via electrostatic interactions, which could trigger Aβ accumulation on lipid membranes.[16] The peptides adsorbed on a 2D brain SLB facilitate increase in the local peptide concentration to induce efficient peptide aggregation. This phenomenon, referred to as macromolecular crowding, favors peptide self-association as a thermodynamic and kinetic consequence.[17,18]

3.3.2. Imaging of Aβ aggregates incubated with various sizes of AuNPs on brain SLB. First, AuNPs of various sizes (20, 50, or 80 nm) were co-incubated with 25 μM of Aβ monomers on the brain SLB for 6 hr and 48 hr. It was previously reported that 50 pM of 50-nm AuNP solution could induce plaque-like Aβ structures.[9] We calculated the total surface area of 50 pM of 50-nm AuNPs and adjusted the concentrations of 20-nm and 80-nm AuNPs to retain the same total surface area in each case. In other words, 312.5 pM of 20-nm AuNPs and 19.53 pM of 80-nm AuNPs were incubated with Aβ on the brain SLB. Aβ aggregates such as Aβ oligomers, spherical aggregates, protofibrils, and fibrils are typically named for their size and structure. Aβ oligomers have a height of 2–3 nm and a width of 5–25 nm, and spherical aggregates with diameters ranging from 15–35 nm have 200–400 monomers. Protofibrils have a width of 6–10 nm and a length ranging from 5–160 nm, whereas fibrils are filamentous structures with a width of ~10 nm and a length of 0.1–10 μm.[2,19] After 6 hr of incubation of Aβ with 20-nm, 50-nm, or 80-nm AuNPs, they mainly formed protofibrils and short fibrils on the brain SLB; under dark-field microscopy, the color of the Aβ aggregates varied with particle size (Figure 3.2). When plasmonic AuNPs are brought close to each other, the plasmonically coupled AuNPs generate color changes based on plasmon resonance wavelength shifts.[20] In the case of 20-nm AuNPs, the co-aggregates appeared green in the dark-field images, suggesting that nanoparticles had not aggregated after 6 hr (Figure 3.2).

This implies that 20-nm AuNPs did not accumulate, but remained dispersed inside small Aβ aggregates. This was further supported by the TEM image shown in Figure 3.2a; most 20-nm AuNPs were positioned close to each other and the AuNPs had formed protofibrils. In contrast, the larger 50-nm AuNPs induced formation of much larger Aβ aggregates, accompanied by dark-field color changes from green to greenish yellow (Figures 3.2a). In the case of 80-nm AuNPs, noticeably more Aβ aggregates were formed after 6 hr (Figure 3.2a). When Aβ was incubated with 20-nm AuNPs for 48 hr (Figure 3.2b), more protofibrils and short fibrils were observed, and a higher number of Aβ-modified nanoparticles were observed, but they remained well dispersed. For 50-nm AuNPs, small plaque-like structures were formed with more densely modified nanoparticles. In the case of 80-nm AuNPs, many particles were densely modified to Aβ aggregates, as shown in Figure 3.2b and large plaque-like structures were formed, with a dark-field color change to a reddish yellow color. Our results suggest that higher nanoparticle density results in larger Aβ aggregates. Because Aβ growth can be influenced by the accumulation of Aβ peptides on solid surfaces, we measured the amount of Aβ adsorbed on each AuNP. The 20-nm, 50-nm, and 80-nm AuNPs were measured before and after 30-min co-incubation with Aβ using the dynamic light scattering (DLS) (Zetasizer, Malvern, Worcestershire, UK). The size of nanoparticles increased due to Aβ aggregations on nanoparticle surfaces, and larger particles induced more Aβ aggregation on particle surfaces (data nor shown). The size increase was also found to be correlated with the amount of Aβ peptides adsorbed on nanoparticle surface. The results indicate that the local concentration of amyloidogenic peptides plays a key role in the Aβ growth mechanism.[11] The increased local concentration of proteins at the surface of nanoparticles could enhance the probability of partially unfolded proteins coming into frequent contact, resulting in more rapid clustering of nanoparticles and proteins.[21] In addition, it has been reported that spherical particles in protein solution are likely to form clusters, owing to short-

range attraction induced by the depletion effect and the weakly screened electrostatic repulsion resulting from the modest charge.[22,23]

3.3.3. Measurement of structural changes in Aβ-AuNP co-aggregates using SERS and CD.

We studied how Aβ secondary structures affected after incubation with AuNPs on the brain SLB using SERS and CD spectra (Figure 3.3). We measured SERS signals to investigate the interactions between Aβ and AuNPs - the adsorption of molecules onto metal surfaces result in the SERS through electromagnetic field enhancements.[24-26] Therefore, the SERS analysis could elucidate which specific residues of Aβ are strongly bound to the AuNP surface. In the case of 20-nm and 80-nm AuNPs (Figure 3.3a and 3.3c), no significant changes were observed on the surface of the AuNPs. Several peaks were assigned to random coil structures, CH_2 symmetric rocking, CH_2, CH_3 deformation, the S=O of Met, and the COO^- stretching of Asp and Glu. Interestingly, 50-nm AuNPs induced different Raman signals - after 6 hr of incubation, random coil structures as well as β-sheet and α-helix structures were clearly observed (Figure 3.3b). It appeared that conformational changes in Aβ peptides, from random coils to β-sheets or α-helices, were more prevalent on the surface of 50-nm AuNPs than 20-nm and 80-nm AuNPs. These results were further compared to the CD to study changes in protein secondary structures.[27] We used 1-mm quartz cells containing the SLB, incubated under the same conditions used for the dark-field and TEM imaging experiments. After 6 hr of incubation, random coil structures were prevalent in the Aβ aggregates containing 20-nm, 50-nm, and 80-nm AuNPs; many Aβ peptides were stacked on the surface of the AuNPs (Figure 3.3d). With a short incubation time, fewer folded structures contained β-sheets, even though co-aggregates with protofibrils were observed. These results are supported by a

previous report, which stated that random coil structures were mainly observed following co-incubation with AuNPs,[9] resulting from structural perturbation of the surface-bound state of the protein.[28] Under these conditions, adsorbed Aβ peptides are strongly constrained, in quasi-2D, and therefore favor conversion into random coils as opposed to free Aβ monomers.[29,30] In the case of 50-nm AuNPs, the number of β-sheet structures increased and the number of α-helix and random coils decreased as incubation time increased. The 20-nm and 80-nm AuNPs samples formed fewer α-helices or β-sheets and more random coils, but the amount of β-sheet structures increased slightly as incubation time increased (Figure 3.3e). Thus, the 20-nm AuNPs could not act as nucleation seeds within a short incubation time and were not sufficient to form entangled co-aggregates with Aβ, inducing protofibrils and short fibrils owing to the small surface area and low volume fraction of the particles. However, both the 50-nm and 80-nm AuNPs could shorten the lag phase of Aβ aggregation, and 50-nm AuNPs in particular showed the potential to increase growth of Aβ folded structures rich in β-sheets, with plaque-like structures in which Aβ and AuNPs clustered together. These plaque-like structures were similar to amyloid plaques in the AD brain, which are composed of interwoven masses of fibrils.[31] Co-incubation of 80-nm AuNPs showed that larger nanoparticles inhibit Aβ aggregation, even though the particles' larger surface area provided more binding sites for nucleation. It should be noted that Aβ aggregates grown on the surface of 80-nm AuNPs have lower percentage of β-sheet than 50-nm AuNPs. 80-nm AuNPs with the surface-bound Aβ peptides tend to be more clustered to form large Aβ aggregates than the 50-nm AuNP case, and slight increase in both α-helix and random coil structures was observed in the CD data for 80-nm AuNPs. Moreover, based on the Raman data (Figure 3.3b), the conformational changes of Aβ peptides from random coils to β-sheets or α-helices were more dominant for 50-nm AuNPs than 80-nm AuNPs. The results suggest that Aβ aggregates have more β-sheet structures in the case of 50-nm AuNPs while 80-nm AuNPs induce more

alpha helix and random coil structures in Aβ aggregates, forming more amorphous peptide aggregates. The largely clustered 80-nm AuNPs induce AuNP aggregation-driven Aβ-AuNP co-aggregate structures while 50-nm AuNPs simply offer Aβ aggregation platforms and the aggregation between Aβ peptides are more prevalent in this case.

3.3.4. Aβ-AuNP co-aggregates formation with differently surface-charged AuNPs.

It has been reported that AuNPs with modified surface charges can alter the Aβ aggregation pathway and induce differing cytotoxicity to neuroblastoma cells.[32] To investigate how surface charge influences Aβ aggregation, amine-modified AuNPs (amine-AuNPs) with positive charges were synthesized (see Supplementary Fig. S4 and Supplementary information for additional details) and compared with citrate-modified AuNPs (citrate-AuNPs) with negative charges (BBI Solutions OEM Ltd., Cardiff, UK) in terms of their effects on Aβ growth. Both types of nanoparticles were 40 nm in size, with the same molar concentration. To maintain the same total surface area, 75 pM of 40-nm AuNPs were used as equivalent to the total area of 50 pM of 50-nm AuNPs. First, we captured dark-field and TEM images after 6 hr and 48 hr of incubation, to detect clustering of AuNPs and determine the structure of Aβ co-aggregates with AuNPs (Figure 3.4). In the dark-field images, after incubation for 6 hr, no clear differences between the two samples were observed, but the color and size of the aggregates could be discriminated after 48 hr of incubation. Citrate-AuNPs formed larger Aβ aggregates by gathering more peptides and AuNPs together, whereas amine-AuNPs formed smaller aggregates. The TEM data (Figure 3.4a) showed that Aβ and clustered amine-AuNPs formed small amorphous aggregates; it appears that the Aβ peptides could not form protofibrils. As mentioned, there were six negatively charged residues (D1, E3, D7, E11, E22, and D23) and three positively charged residues (R5, K16,

and K28) in Aβ sequence, and therefore the electrostatic interactions between positively charged AuNPs and Aβ would be stronger, which could result in electrolyte-induced aggregation followed by misfolding of peptides, inhibiting further fibrillization.[14,33] Tight interactions between AuNPs and Aβ could limit the structural flexibility of Aβs which is necessary for conformational conversion, and inhibit accommodation of other Aβ monomers on the surface or in solution.[12,34] In other words, Aβ peptides are strongly adsorbed onto the surface of amine-AuNPs and conformational conversion of these surface-bound Aβs would be hindered, resulting in retardation of Aβ aggregation. As incubation time increased, the TEM image showed formation of fibrils with densely packed amine-AuNPs, shown by orange coloring in the correlated dark-field image (Figure 3.4b). However, after 6 hr of incubation of Aβ and citrate-AuNPs, protofibrils or short fibrils were produced around citrate-AuNPs without AuNP clustering (Figure 3.4a). The surface of citrate-AuNPs was mostly covered by surface-bound 40-nm Aβ peptides, and these citrate-AuNPs could then act as nucleation seeds of further aggregation by increasing the local concentration of Aβs, with fewer constraints on conformational conversion. Based on the short lag phase, Aβ aggregation was accelerated by agglomeration of AuNPs. Similar results were observed for the citrate-AuNPs in the dark-field and TEM images as were observed for the previously mentioned co-incubation with 50-nm AuNPs, forming Aβ and AuNPs co-aggregates in close proximity (Figure 3.4). We next examined surface how particle charge affects Aβ secondary structures after co-incubation (Figure 3.5). The net charge of Aβ is negative at a physiological pH (pI of Aβ = pH 5.2),[35] so the surface charge of nanoparticles will be negative when Aβ monomers were attached. Given these results, amine-AuNPs interacted with Aβ peptides through electrostatic interactions between the negatively charged amino acids and the functional groups on the surface of AuNPs. In addition, amine-AuNPs covered by Aβ peptides would have negative charges, leading to clustering of amine-AuNPs owing

to the strong electrostatic interactions. In contrast, citrate-AuNPs have negatively charged surfaces, and a reason for Aβ binding to citrate-AuNPs is Aβ-AuNP complex formation involving the replacement of the citrate groups on AuNPs with Aβ peptides and the direct attachment of AuNPs to Aβ peptides.[9]

3.3.5. Detection of interaction sites in Aβ and secondary structures of Aβ-AuNP co-aggregates.

To reveal the structural changes in Aβs on the surface of AuNPs, time-lapse SERS signals were collected during incubation. As seen in Figure 3.5a, although the SERS signals of amine-AuNPs did not differ after incubation for 2 hr and 4 hr, predominantly showing CH_2 symmetric rocking, CH_2, CH_3 deformation, the S=O of Met, and the COO^- stretching of Asp and Glu, the results indicate that some residues were in close contact with the surface of AuNPs. Amino acids containing aromatic residues such as Phe and Tyr, and nonpolar residues such as Met, Val, and Ile could directly interact with the surface of the metal. The hydrophobic residues (Phe, Ile, Val, and Gln) and Lys of Aβ peptides were likely bound to the surface of amine-AuNPs, which could hinder conformational changes into cross β-sheet structures. As incubation time increased to 6 hr, amine-AuNPs aggregated due to the negative charge of Aβ residues, followed by increased interaction of Aβ peptides on the surface of clustered AuNPs with stronger SERS signals. In contrast, as shown in Figure 3.5b, the SERS peaks of Aβ peptides on the surface of citrate-AuNPs were independent of the incubation time; they showed some peaks indicating CH_2 symmetric rocking, CH_2, CH_3 deformation, the S=O of Met, and the COO^- stretching of Asp and Glu due to formation of Aβ and citrate-AuNP complexes through exchange of citrate ligands for negatively charged Aβ residues. Both amine-AuNPs and citrate-AuNPs clearly showed peaks at 1254 cm^{-1} after 2 hr

incubation, representing the formation of random coil Aβ peptide structures. It could be concluded that the Gln and Lys residues and hydrophobic residues such as Phe, Ile, and Val of Aβ peptides were preferentially bound to the surface of amine-AuNPs, which may have inhibited conformational change of Aβ into cross β-sheet structures, resulting in spherical aggregates after 6 hr of incubation. Compared to the amine-AuNP case, Aβ peptides on the surface of citrate-AuNPs showed less diverse SERS peaks with random coil feature as well as Asp and Glu residue features. The results indicate the easier conformational change of the Aβ peptides to β-sheet structures within the same incubation time is possible for the citrate-AuNP case.

The CD results (Figure 3.5c) shows that amine-AuNPs co-incubation produced fewer β-sheet structures than co-incubation with citrate-AuNPs for 6 hr or 48 hr. As shown in the TEM images in Figure 3.4, after 6 hr, amine-AuNPs induced small amorphous Aβ aggregates, with fewer α-helix or β-sheet structures and more random coils, and, after a longer incubation, fibril structures were branched from the clustered amine-AuNPs. Those amorphous aggregates consisted of β-sheet structures and might represent intermediate stages of Aβ elongation and aggregation. This result was concordant with the CD spectra, which showed that the number of β-sheet structures increased as incubation time increased. Citrate-AuNPs acted as nucleation seeds, reducing the lag time, so protofibrils were formed after 6 hr and further aggregation occurred as incubation time increased, producing more β-sheet structures. Finally, the surface charge of nanoparticles can greatly influence Aβ growth and control their conformation, causing changes in secondary structures.

3.3.6. Observing Aβ aggregates formed with different shapes of Au nanostructures.

Next, how particle shape affects Aβ aggregation on the brain SLB was studied by comparing

spherical AuNPs, anisotropic gold nanorods (AuNRs) and multi-facted gold nanocubes (AuNCs). All these particles were modified with amine functional groups, providing positively charged surfaces. It should noticed that tuning the aspect ratio of AuNRs or truncating AuNCs produces resonance peaks in the near-IR region (700–1300 nm), useful range for in vitro sensor and in vivo imaging/therapeutic applications.[36, 37] We synthesized AuNRs and AuNCs with one side of a similar length, and the long axis of the AuNRs and the edge of the AuNC were approximately 50 nm, to facilitate comparison of their structural effects. The morphology and color of Aβ aggregates with AuNRs or AuNCs were examined via dark-field microscopy and TEM (Figure 3.6). AuNRs generate LSPR effects at two distinct wavelengths that correspond to the longitudinal mode and the transverse mode in the near-IR region (700–1300 nm) at an appropriate aspect ratio.[38, 39] In this study, the aspect ratio of AuNRs was approximately 3.17, showing a longitudinal mode LSPR peak in the near-IR region,[39] so light was scattered at approximately 520 nm owing to the transverse mode employed for dark-field imaging. The AuNRs had a short axis of 13.55 nm and a long axis of 42.96 nm; the length of the edge of the AuNCs was 51.05 nm. The particles were uniform, and green colors were obtained under dark-field microscopy. In this experiment, the total surface area of the AuNRs and the AuNCs remained the same via adjustment of the concentration of the nanoparticles. When AuNCs are compared to spherical AuNPs, larger aggregates were formed on AuNCs than on AuNRs mainly because AuNCs have a larger effective surface area with more isotropic structures than AuNRs. However, it should be also noted that, although spherical AuNPs are more isotropic, the aggregates grown on AuNPs displayed poorer structure and lower percentage of β-sheet than AuNCs. This is because the β-sheet-aggregation-inducing amino acids in Aβ peptide, Phe, Tyr, Met, Val and Ile, closely interacted with AuNPs (Figure 3.5a), and this hindered the formation of β-sheet-stacking-based Aβ aggregates while AuNCs did not interact with β-sheet-aggregation-inducing amino

acids.

The dark-field scattering color of Aβ peptides, co-incubated with AuNRs for 6 hr, was green, but the color was changed to orange after 48 hr incubation (Figure 3.6a). This indicates that AuNRs were aggregated after 6 hr of involvement in Aβ growth. To detect aggregate states, we obtained the TEM images for the same samples, and concluded that AuNRs had relatively weak interactions with Aβ peptides, resulting in smaller aggregates after 6 hr of incubation and a few fibrils after 48 hr of incubation (Figure 3.6). It was reported that cetyltrimethylammonium bromide (CTAB) specifically binds to {100} faces, along the length of rods and forms positively charged surface of AuNRs,[40] and it is likely that Aβ was preferentially bound to the long axis surface of AuNRs. When AuNRs of a different aspect ratio were incubated with Aβ for 48 hr, there were no noticeable changes in the morphology of the Aβ co-aggregates.

Figure 3.6a and 3.6b show the results of incubation of AuNCs with Aβ for 6 hr and 48 hr, respectively; the distinct scattering signals in the dark-field images resulted from the strong LSPR properties of AuNCs.[41] Although the edge length of the AuNCs is similar to the long axis length of the AuNRs, the AuNCs have a larger effective surface area with more isotropic structures than AuNRs. Long Aβ fibrils were observed within 6 hr with AuNCs. In the dark-field images, the color changed to yellowish green or yellow after 6 hr of incubation, followed by a more red-shifted to orange color in some cases after 48 hr incubation. In addition, the morphology of Aβ-AuNC co-aggregates was observed to be networks with distinguishable and entangled fibrils that would likely be rich in β-sheet structures. Aβ could bind to AuNCs in different directions, facilitating Aβ growth on the surface of AuNCs. Thereafter, Aβ peptides were grown on six-faceted AuNCs, resulting in a more rapid nucleation process; Aβ fibrils were interwoven, resulting in networks of fibrils with AuNCs

(Figure 3.6b).

3.3.7. SERS and CD measurement for detecting interaction sites and secondary structures of Aβ aggregates.

We then investigated both their secondary structural features of Aβ aggregates and interaction between Aβ and the surface of Au nanostructures in more details (Figure 3.7). The structure of Aβ aggregates is dependent on the initial local concentration. Hence, the adsorption isotherms were obtained for AuNRs and AuNCs with spherical AuNPs functionalized with amine groups. Incubation with AuNCs differed from that with AuNRs or AuNPs in that the curve showed a maximum equilibrium surface concentration, and the adsorbing and desorbing constant for Aβ peptides on AuNCs reached equilibrium in the same incubation period. The shape of the adsorption isotherm indicated an adsorption affinity for peptides, and the maximum amount of adsorbed molecules and binding affinity could be determined after equilibrium was reached.[42] This result also supported that the initial concentration of Aβ peptides on the surface could be an important factor.[15] Both AuNRs and AuNCs possess positively charged surfaces but AuNRs and AuNCs interacted differently with Aβ at the beginning of incubation, as seen in Figure 3.7a and 3.7b. In the case of AuNRs, several peaks with low intensity, stemming from positively charged or polar residues such as Lys, Arg, Gln, and Asn, and aromatic or nonpolar residues such as Phe, Tyr, Val, and Ile, were detected after 2 hr of incubation, whereas those peaks disappeared as incubation time increased. The SERS signals showed that CH_2 symmetric rocking, CH_2, CH_3 deformation, S=O of Met, and the COO^- stretching of Asp and Glu remained throughout the incubation process, which implies that Aβ peptides were closely bound to the surface of AuNRs within a short time, followed by formation of random coil structures. The residues including Phe, Ile, Val, Gln, and Lys of Aβ peptides were likely bound to the surface AuNRs, and this may inhibit conformational

changes into cross β-sheet structures, resulting in rather spherical aggregates after 6 hr incubation. On the other hand, the representative peaks near 1254 cm^{-1} were detected for random coil structures after incubation of Aβ peptides with AuNCs, and no significant incubation-time-dependent changes were observed. The Aβ peptides on the surface of AuNCs only showed several peaks of random coil structures and Asp and Glu residues, and the Aβ peptides were changed to form β-sheet structures after 6 hr incubation. In addition, we could discern secondary structural changes in CD measurements after 6 hr and 48 hr of incubations (Figure 3.7c and 3.7d), strictly correlated with the morphology observed in TEM images. When AuNRs and AuNCs were co-incubated with Aβ for 6 hr, AuNCs accelerated Aβ fibrillization, producing fibrils bound to AuNCs - more β-sheet structures were observed for the AuNC case than the AuNR co-incubation, which showed fewer β-sheet and more α-helix structures (Figure 3.7d). As incubation time increased, Aβ formed fibrils on both samples, but the quantity of fibrils and their structural characteristics were different (Figure 3.7d). The networks of Aβ fibrils with AuNCs were mostly composed of β-sheet and random coil structures, whereas the few fibrils that were bundled with AuNRs contained more random coil structures than β-sheet structures, although the amount of β-sheet structures was increased.

3.3.8. Cell viability assay with SH-SY5Y neuroblastoma cells.

We next studied the cytotoxicity of NP-Aβ aggregates on neuroblastoma cells, and SH-SY5Y neuroblastoma cells were used to perform a cell viability assay using CCK-8 assay kit (Figure 3.8). It was shown that Aβ oligomers are more toxic than Aβ fibrils or plaques, inducing acute cell death.[2,3] Self-assembled Aβ oligomers cause ion dyshomeostasis, membrane permeabilization, oxidative stress to the cell membrane, and synaptotoxicity, and larger Aβ

oligomers or spherical Aβ assemblies of approximately 15 nm could be the elusive toxic species.[43] After Aβ peptides were co-incubated with Au nanostructures for 6 hr and 48 hr, the differently structured aggregates were formed. As shown in Figure 8, after 6 hr of incubation, the Aβ structures without AuNPs were highly toxic, with 43% cell viability, and the Aβ aggregates with amine-AuNPs and AuNRs yielded approximately 51% and 57% cell viabilities, respectively. Spherical Aβ aggregates incubated with amine-AuNPs or AuNRs showed more toxicity to SH-SY5Y cells than the fibrils formed with other types of Au nanostructures. When fibrils with a wide range of lengths were formed with AuNCs and citrate-modified AuNPs, cell viability was increased. As NP-Aβ co-incubation time increased, the toxicity of Aβ aggregates decreased. However, after 48 hr of incubation without Au nanostructures or with 20-nm AuNPs, cell viability was less than 70%. In the case of 20-nm AuNP co-incubation of Aβ on the brain SLB for 48 hr, protofibrils and short fibrils that are toxic to neuroblastoma cells were dominantly formed. In contrast, 50-nm AuNPs, 80-nm AuNPs and citrate-AuNPs induced plaque-like Aβ aggregates. AuNCs also produced the networks of fibrils. Amine-AuNPs and AuNRs induced the formation of fibril bundles while longer fibrils were formed with amine-AuNPs. Au nanostructure-induced mature fibrils or plaque-like structures of Aβ aggregates resulted in the low toxicity (>80% cell viability).

3.4. Conclusion

We showed how the size, shape and surface charge of nanoparticles influence Aβ aggregation and fibrillization on the brain SLB and studied the cytotoxicity of AuNP-Aβ co-aggregates on neuroblastoma cells. Aβ peptides interacted with anionic lipids in the lipid bilayer, showing a macromolecular crowding effect and folding into structures rich in β-sheets on the SLB. It

should be noticed that the size, shape and surface charge of nanoparticles are tunable, and these nanoparticles could be used as drug carriers, photothermal and photodynamic therapeutic tools or inhibitors of Aβ aggregates. Further, Au nanostructures have great utility as imaging tools, in that they generate LSPR effects at specific wavelengths, allowing us to obtain a variety of optical data on the interactions between peptides and nanoparticles. Our results offer a systematic and fundamental understanding on Aβ aggregation with nanoparticles on a fluid membrane platform and facilitate further development of tools for diagnosis and cure of Alzheimer's disease using nanostructures.

3.5. References

1. LaFerla, F.M., Green, K.N. & Oddo, S. *Nat. Neurosci.* **8**, 499–509 (2007).

2. Ross, C.A. & Poirier, M.A. *Nat. Med.* **10**, S10–S17 (2004).

3. Deshpande, A., Mina, E., Glabe, C. & Busciglio, J. *J. Neurosci.* **26**, 6011–6018 (2006).

4. Aisenbrey, C. *et al*. *Eur. Biophys J.* **37,** 247–255 (2008).

5. Kim, S.I., Yi, J.S. & Ko, Y.G. *J. Cell Biochem.* **99,** 878–889 (2006).

6. Kawarabayashi, T. *et al*. *J. Neurosci.* **24,** 3801–3809 (2004).

7. Waschuk, S.A., Elton, E.A., Darabie, A.A., Fraser, P.E. & McLaurin, *J. Biol. Chem.* **276,** 33561–33568 (2001).

8. Matsuzaki, K. *et al*. *Biochim. Biophys. Acta.* **1768,** 122–130 (2007).

9. Lee, H., Kim, Y., Park, A. & Nam, J.-M. *Small* **10,** 1779–1789 (2014).

10. Sonnichsen, C., Reinhard, B.M., Liphardt, J.& Alivisatos, A.P. *Nat. Biotech.* **23,** 741–745

(2005).

11. Cabaleiro-Lago, C., Quinlan-Pluck, F., Lynch, I., Dawson, K.A. & Linse, S. *ACS Chem. Neurosci*. **1,** 279–287 (2010).

12. Cabaleiro-Lago, C. *et al*. *J. Am. Chem. Soc*. **130,** 15437–15443 (2008).

13. Brambilla, D. *et al*. *ACS Nano* **6,** 5897–5908 (2012).

14. Chan, H.-M. *et al*. *Biomaterials* **33,** 4443–4450 (2012).

15. Fei, L. & Perrett, S. *Int. J. Mol. Sci*. **10,** 646–655 (2009).

16. Matsuzaki, K. *Biochim. Biophys. Acta* **1768,** 1935–1942 (2007).

17. Bokvist, M. & Grobner, G. *J. Am. Chem. Soc*. **129,** 14848–14849 (2007).

18. Stefani, M. *Int. J. Mol. Sci*. **9,** 2515–2542 (2008).

19. Ahmed, M. *et al*. *Nat. Struc. Mol. Biol*. **17,** 561–567 (2010).

20. Myroshnychenko, V. *et al*. *Chem. Soc. Rev*. **37,** 1792–1805 (2008).

21. Mahmoudi, M., Kalhor, H.R., Laurent, S. & Lynch, I. *Nanoscale* **5,** 2570–2588 (2013).

22. Poon, W.C.K. *J. Phys. Condens. Matter* **14,** R859–R880 (2002).

23. Stradner, A. *et al*. *Nature* **432,** 492–495 (2004).

24. Dong, J. *et al*. *Biochemistry* **42,** 2768–2773 (2003).

25. Chou, I.-H. *et al*. *Nano Lett*. **8,** 1729–1735 (2008).

26. Choi, I., Huh, Y.S. & Erickson, D. *Microfluid Nanofluid.* **12,** 663–669 (2012).

27. Kelly, S.M., Jess, T.J. & Price, N.C. *Biochim. Biophys. Acta.* **1751,** 119–139 (2005).

28. Bett, C.K. *et al*. *ACS Chem, Neurosci*. **1,** 608–626 (2010).

29. Dobson, C.M. *Nature* **426,** 884–890 (2003).

30. Matthes, D., Gapsys, V. & Groot, B.L. *J. Mol. Biol*. **421,** 390–416 (2012).

31. Friedricha, R.P. *et al*. *Proc. Natl. Acad. Sci. U.S.A*. **107,** 1942–1947 (2010).

32. Liao, Y.H., Chang, Y.J., Yoshiike, Y., Chang,Y.C. & Chen, Y.R *Small* **8,** 3631–3639 (2012).

33. Rauk, A. *Chem. Soc. Rev*. **38,** 2698–2715 (2009).

34. Wang, Q. *et al*. *Phys. Chem. Chem. Phys.* **13,** 15200–15210 (2011).

35. Yokoyama, K. & Welchons, D.R. *Nanotechnology* **18,** 105101 (2007).

36. Adura, C. *et al*. *ACS Appl. Mater. Interfaces.* **5,** 4076−4085 (2013).

37. Shi, P., Li, M., Ren, J. & Qu, X. *Adv. Funct. Mater*. **23,** 5412–5419 (2013).

38. Boisselier, E. & Astruc, D. *Chem. Soc. Rev*. **38,** 1759–1782 (2009).

39. Ng, K.C. & Cheng, W. *Nanotechnology* **23,** 105602 (2012).

40. Murphy, C. J. *et al*. Anisotropic metal nanoparticles: synthesis, assembly, and optical applications. *J. Phys. Chem. B.* **109,** 13857-13870 (2005).

41.Wu, X. *et al*. *ACS Nano* **4,** 113–120 (2010).

42. Roach, P., Farrar, D. & Perry, C.C. *J. Am. Chem. Soc.* **128,** 3939–3945 (2006).

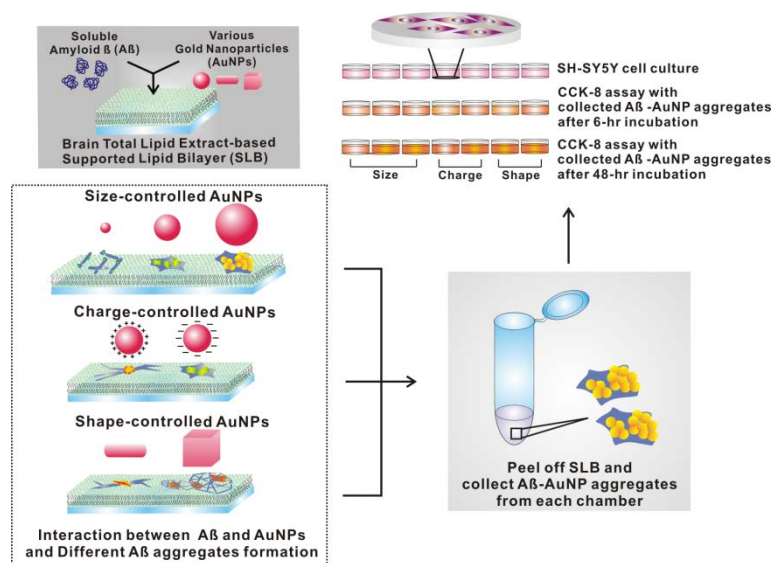43. Benilova, I., Karran, E. & Strooper, B.D. *Nat. Neurosci*. **15,** 349–357 (2012).

Figure 3.1. Schematic illustration of the formation of Aβ and gold nanoparticle (AuNP) co-aggregates on the total brain lipid-based supported lipid bilayer and cell viability assay with various Aβ aggregates. Depending on the size, charge, and shape of AuNPs, different Aβ aggregate structures can be formed.
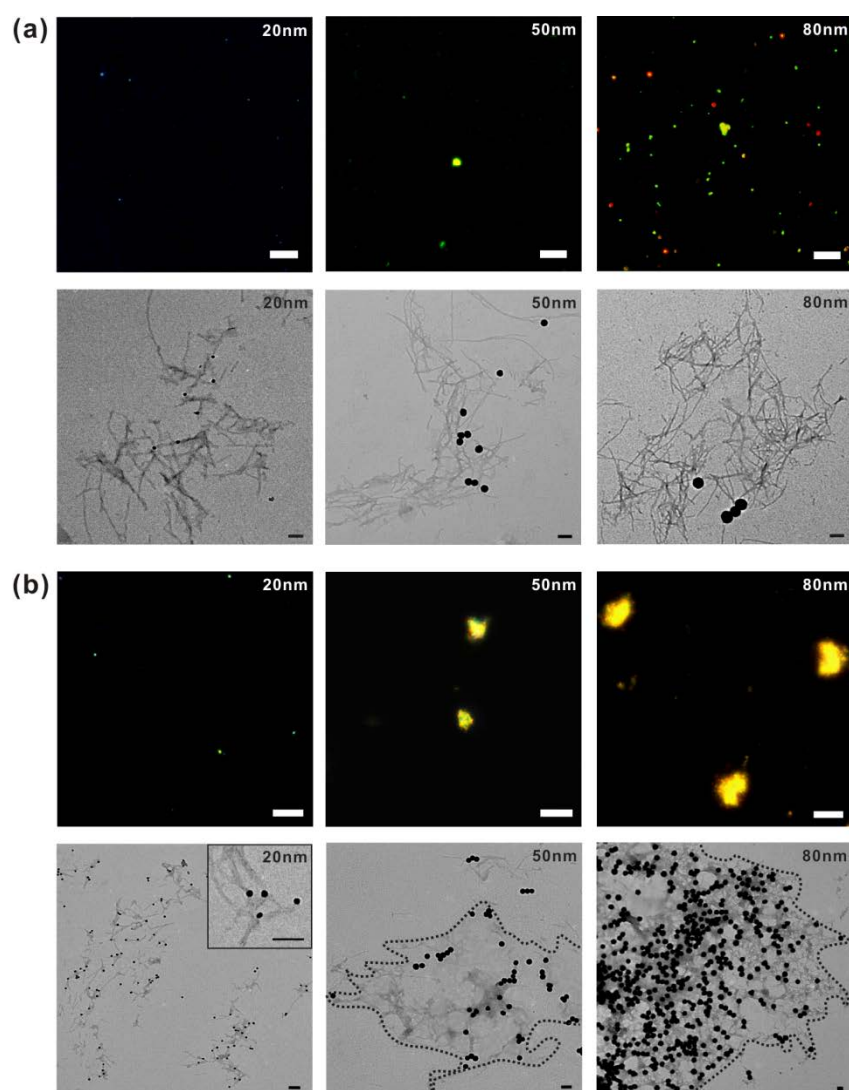
Figure 3.2. The dark-field and TEM images of Aβ aggregates with various sizes of AuNPs [20-nm AuNPs (left), 50-nm AuNPs (middle), and 80-nm AuNPs (right)] on the brain SLB. The images were obtained after the co-incubation of Aβ and AuNPs for (a) 6 hr and (b) 48 hr. The inset figure in (b) shows a magnified image for the 20-nm AuNP case. It should be noted that the dark-field images of 20-nm AuNPs are difficult to be obtained. The scale bars in all the dark-field images are 10 μm and those in TEM images are 100 nm.

72

Figure 3.3. Analysis on the interactions between Aβ and AuNPs and the secondary structures of Aβ aggregates. The surface-enhanced Raman scattering (SERS) spectra of Aβ on the surfaces of (a) 20-nm AuNPs, (b) 50-nm AuNPs, and (c) 80-nm AuNPs with varying incubation time. Circular-dichroism (CD) measurements and secondary structure analysis after co-incubation of Aβ and AuNPs for (d) 6 hr and (e) 48 hr. The error bars were calculated with three individual samples.
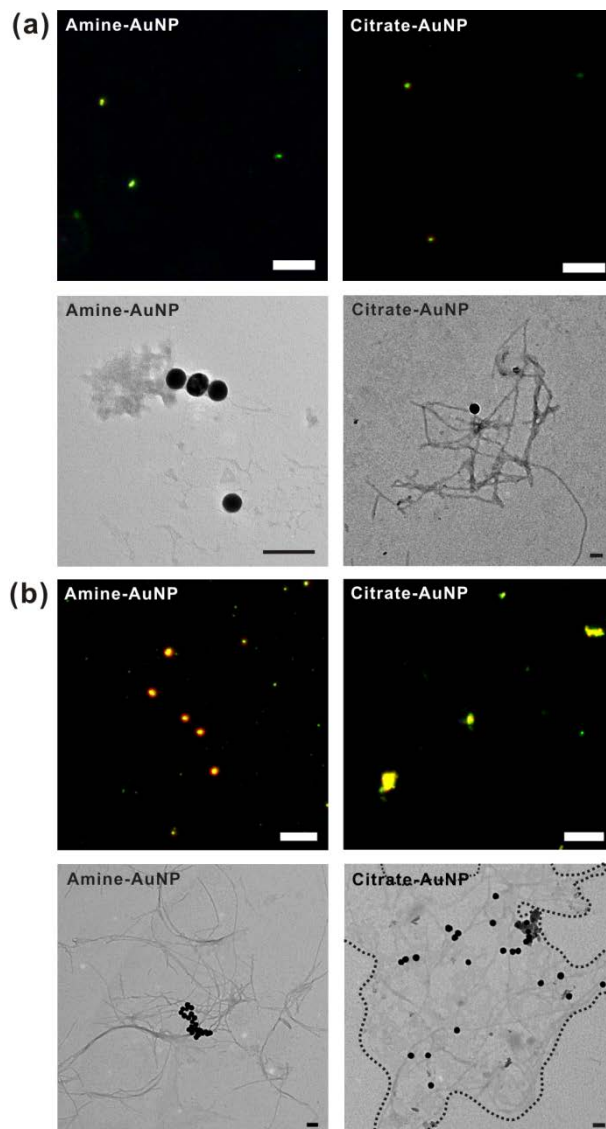
Figure 3.4. The dark-field and TEM images of Aβ-AuNPs co-aggregates with positively or negatively-charged AuNPs on the brain SLB after 6-hr and 48-hr co-incubation. Aβ and 40-nm AuNPs were co-incubated for (a) 6 hr and (b) 48 hr. The scale bars in the dark-field images are 10 μm whereas those in the TEM images are 100 nm.
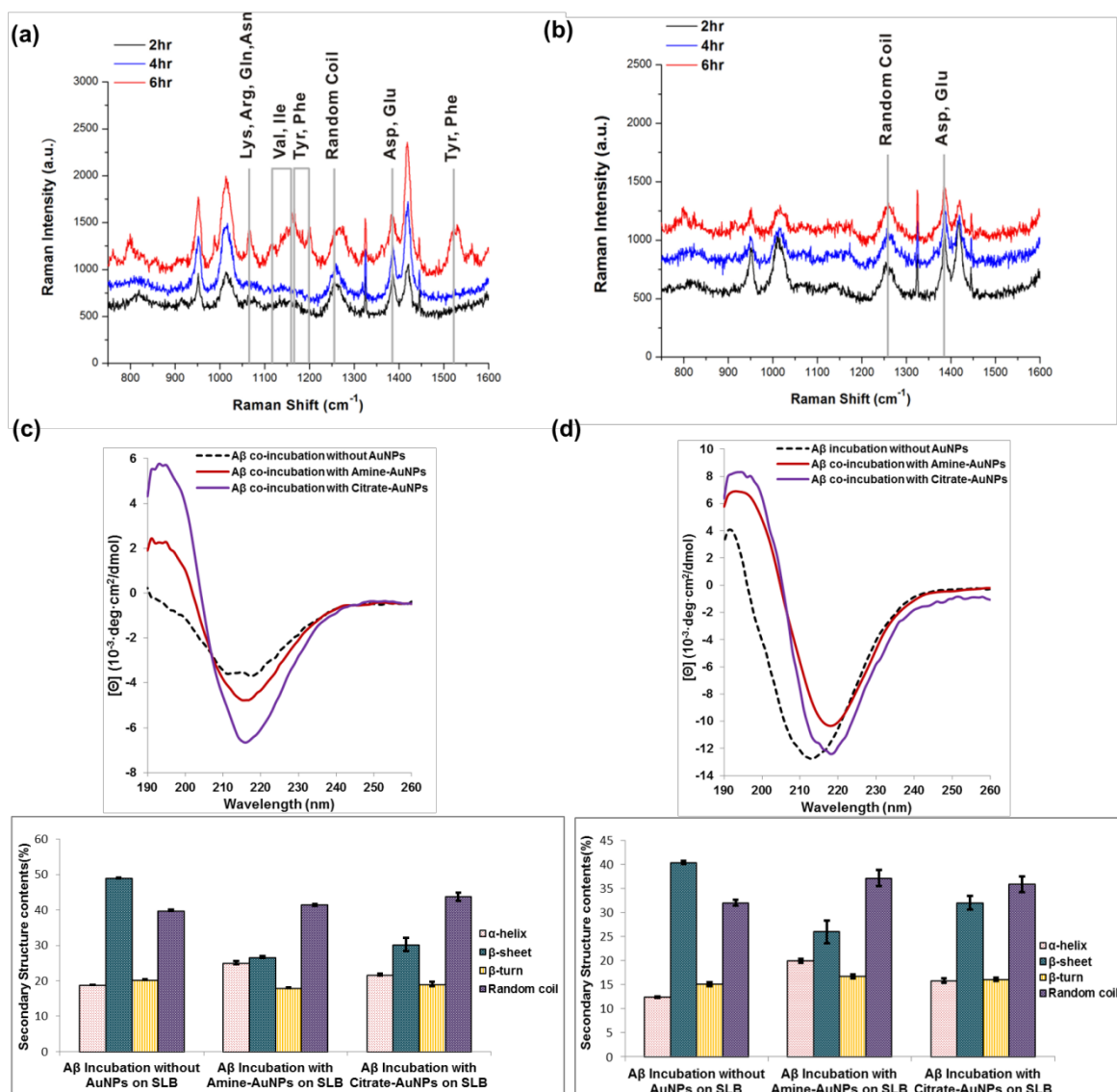
Figure 3.5. Study on the interactions between Aβ and differently-charged AuNPs and secondary structural analysis of Aβ aggregates. (a) The SERS spectra from time-lapse incubation of Aβ and amine-AuNPs. (b) The SERS spectra of Aβ on the surface of citrate-AuNPs with varying incubation time. The CD spectra show the secondary structures of Aβ aggregates incubated with AuNPs for (c) 6 hr and (d) 48 hr. The error bars were calculated with three independent samples.
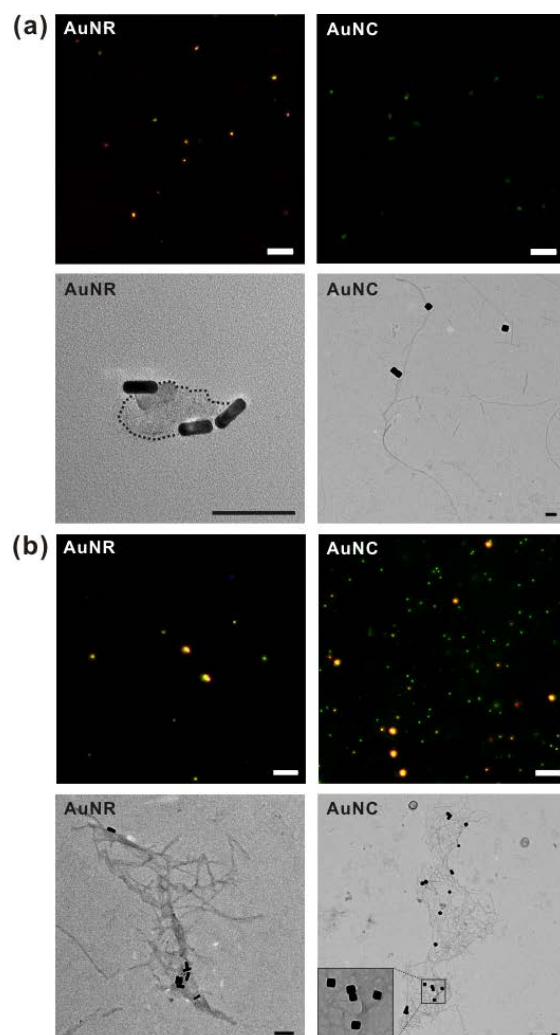
Figure 3.6. The dark-field and TEM images for Aβ aggregates incubated with AuNRs and AuNCs on the brain SLB. The image were obtained after (a) 6-hr incubation and (b) 48-hr incubation. The scale bars of the dark-field images are 10 μm and those of the TEM images are 100 nm.
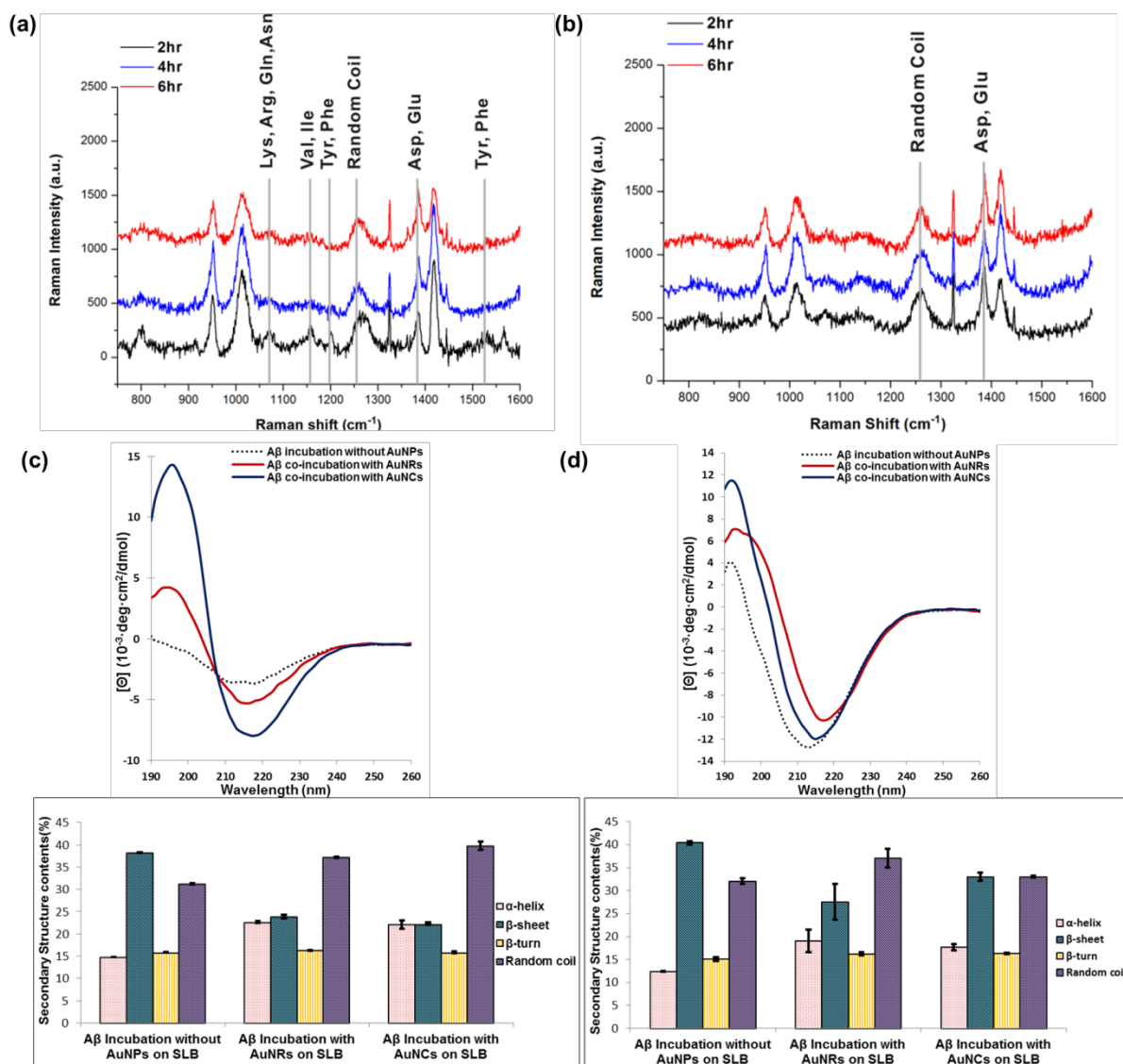
Figure 3.7. Analyses on the interactions between Aβ and differently-shaped nanoparticles and secondary structural analysis of Aβ aggregates. The SERS signals were measured after time-lapse incubation for (a) AuNRs and (b) AuNCs. The CD spectra show the secondary structures of Aβ aggregates incubated with AuNRs or AuNCs for (c) 6 hr and (d) 48 hr. The error bars were calculated with three individual replicates.
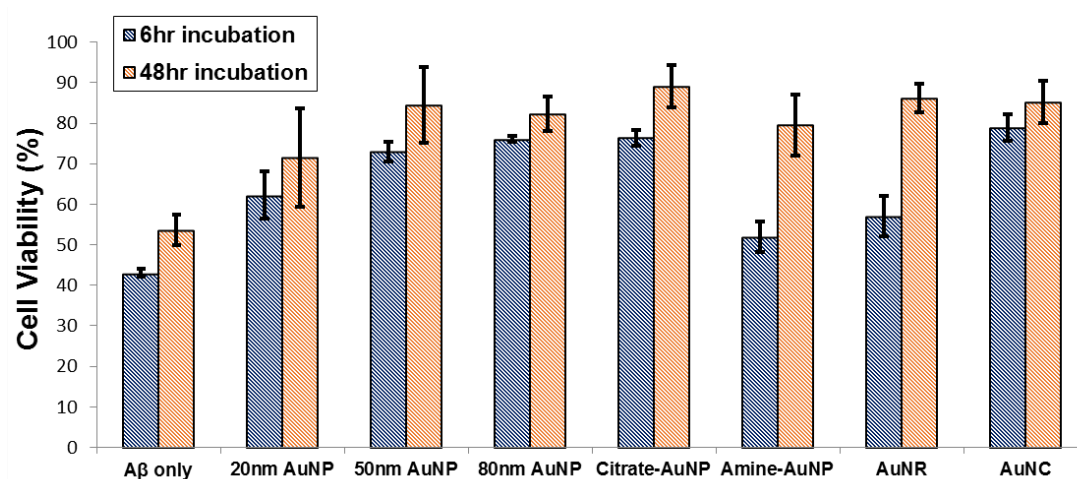
Figure 3.8. Cell viability assay of Aβ aggregates formed after 6-hr and 48-hr incubation with SH-SY5Y neuroblastoma cells using CCK-8 assay. After 6-hr and 48-hr incubation of Aβ and Au nanostructures on the brain SLB, the collected Aβ aggregates were incubated with SH-SY5Y cells at a concentration of 1.0×10^4 cells/well in 96-well plates. The error bars were calculated with three individual replicates.

국 문 초 록

세포는 세포막을 이용해 세포 외부환경과의 물리적인 장벽을 형성하고 세포 내 생체 물질과 세포 소기관들을 보호하고자 한다. 세포막은 대부분이 인지질 이중층으로 형성되어 있으나 세포막 표면은 탄수화물 (carbohydrate), 다양한 종류의 단백질 (protein) 등이 개질되어 있으며 세포막을 관통하는 막단백질 (transmembrane protein), 이온 채널 (ion channel) 등 매우 다양한 생체 분자들이 결집된 집단이다. 이러한 나노 수준의 크기를 갖는 생체 분자들과 세포 소기관의 작용으로 세포는 외부 환경 및 주변 세포들과 상호작용하고 세포 대사활동이 가능하다. 다양한 질병의 원인을 살펴보면 세포막 근처에서 발생하는 생체 분자간 상호작용의 방해 혹은 세포-세포간 비정상적인 상호작용 등에 의한 경우가 많으며, 특히 퇴행성 뇌질환의 경우 뇌 세포막 주변에서 특정 발병 단백질이 자기조립을 형성하면서 세포에 독성을 미치고 뇌세포 사멸 및 뇌 신경 장애를 초래하는 것으로 잘 알려져 있다. 따라서, 본 학위논문에서는 뇌세포 환경을 모사한 인공 세포막을 제작하여 대표적인 퇴행성 뇌질환의 병변 단백질인 아밀로이드 베타의 자기조립 형성을 관찰하고, 나노 물질을 이용하여 자기조립 과정을 조절하여 세포에 미치는 독성을 알아보고자 하였다.

제 1장에서는 다양한 나노 물질을 이용하여 펩타이드, 효소, 질병 관련 단백질 등 생체 분자들의 상호작용을 분석하고 이를 바탕으로 생체 분자간 응집체 형성 조절 등에 대해 설명하고자 한다. 더불어, 체내 세포막을 모사한 인공세포막을 이용하여 막단백질을 비롯한 다양한 단백질에 대한 바이오 센서 및 단백질 응집체 형성 조절 등에 대해 알아보고, 나노 입자와 인공세포막을 결합한 새로운 플랫폼을 기반으로 실제 세포를 도입하여 세포막 단백질과의 상호작용 등에 대하여 설명하고자 한다.

제 2장에서는 뇌조직에서 추출한 세포막 성분을 이용하여 in vitro 상에서 유사한 성질의 세포막을 구현하고, 뇌환경 모방 인공세포막을 기반으로 아밀로이드 베타의 자기조립 형성 과정을 관찰하고자 하였다. 아밀로이드 베타는 세포막과 상호작용하여 베타병풍구조가 많은 소섬유를 형성하고 더 진행되면 소섬유들이 엉킨 플라그 형태의 단백질 응집체가 뇌세포 바깥에 형성되는 것으로 알려진 바 있다. 본 연구에서는 아밀로이드 베타의 자기조립과정인 소섬유 응집체 형성과정을 좀더 자세히 관찰하기 위하여 금나노입자와 암시야 현미경을 이용하여 시간별로 자기조립과정을 이미징하였다. 금나노입자는 특정 파장대의 빛을 산란하는 특성을 갖고 있기에 암시야 현미경을 이용하면 산란되는 빛의 신호만 받아들여 장시간동안 안정적인 이미징이 가능하다. 또한, 금나노입자를 아밀로이드 베타와 공동 배양을 하는 경우, 금나노입자로 인해 아밀로이드 베타의 자기조립 형성에 영향을 주어 소섬유를 이루지 못하고 15 μm 이상의 크기를 갖는 플라그 형태의 응집체가 형성됨을 확인할 수 있었다. 결과적으로 금나노입자를 이용하면 아밀로이드 베타의 자기조립 과정을 효과적으로 관찰할 수 있을 뿐 아니라, 공동 배양 시스템을 통하여 자기조립 조절을 통해 플라그 형태의 응집체 형성을 유도할 수 있었다.

제 3장에서는 상기 제시한 뇌환경 인공세포막에서 금나노입자를 이용하여 아밀로이드 베타의 자기조립 조절이 가능함을 바탕으로 금나노입자의 크기, 표면전하, 모양 등을 달리한 7 종류의 금나노입자를 도입하여 이들과 아밀로이드 베타의 상호작용 분석 및 그 결과로 형성된 각 응집체들이 세포에 미치는 독성에 대해 설명하고자 한다. 20 nm, 50 nm, 80 nm 크기의 구형의 금나노입자를 표면적이 같도록 농도를 조절하여 같은 농도의 아밀로이드 베타와 배양하였고 금나노입자의 크기에 따라 표면에 아밀로이드 베타가 상호작용하는 아미노산 종류가 달라지게 되고, 금나노입자의 크기로 인한 응집현상 촉진에도 영향을 미쳐 서로 다른 형태의 아밀로이드 베타-금나노입자 응집체 형성을 유도할 수

있었다. 금나노입자의 표면전하가 양전하인 경우와 음전하인 경우 특히 초기에 아밀로이드 베타가 금나노입자 표면에 붙은 아미노산의 종류와 개수가 매우 다르게 나타났고 양전하를 나타내는 금나노입자는 베타병풍구조를 저해하고 작은 응집체가 형성되는 것에 매우 기여하는 것으로 나타났다. 마지막으로, 막대형과 정육면체형 금나노입자를 아밀로이드 베타와 같이 배양한 경우에도 나노입자의 형태로 인해 아미노산 상호작용이 다른 것을 확인할 수 있었고, 막대형 금나노입자가 작은 응집체를 형성하여 베타병풍 구조 저해 효과가 더 크게 나타남을 발견하였다. 이는 원이색성분산계와 라만 현미경을 활용한 SERS 측정으로 펩타이드의 2차구조 및 아미노산 잔기에 대하여 분석하여 금 나노입자와 아밀로이드 베타의 상호작용에 대한 정성 및 정량분석이 가능하였다. 이렇게 7종류의 금 나노입자를 통해 6시간, 48시간 배양 후 형성된 14 종류의 아밀로이드 베타-금나노입자 응집체가 neuroblastoma 세포주인 SH-SY5Y에 어떠한 영향을 미치는지에 대한 독성 연구도 진행하였으며, 응집체의 2차 구조에서 베타 병풍 구조가 많이 나타날수록 뇌세포에 가장 세포독성이 큰 것으로 관찰되었다. 이는 기존의 자기조립 과정에서 올리고머, 소섬유, 섬유 다발 등 베타 병풍구조로 인해 형성되는 구조들이 뇌세포에 가장 큰 독성을 나타내며, 금나노입자로 인해 플라그 형태의 큰 응집체를 갖게 되면 베타 병풍구조에 의한 아밀로이드 베타 응집현상이 저해되어 세포 외부에서 신호 교란 및 세포막 파괴 등에 의한 독성이 작아지는 것으로 결론지을 수 있다.